SOURCE DATA TRANSPARENT PROCESS OPEN ACCESS

The Ebola virus VP40 matrix layer undergoes endosomal disassembly essential for membrane fusion

Sophie L Winter[1,2] , Gonen Golani[2,3] , Fabio Lolicato[4,5] , Melina Vallbracht[1,2],
Keerthihan Thiyagarajah[1,2] , Samy Sid Ahmed[6], Christian Lüchtenborg[4], Oliver T Fackler[6,7] ,
Britta Brügger[4], Thomas Hoenen[8] , Walter Nickel[4] , Ulrich S Schwarz[2,3] & Petr Chlanda[1,2,*]

Abstract

Ebola viruses (EBOVs) assemble into filamentous virions, whose shape and stability are determined by the matrix viral protein 40 (VP40). Virus entry into host cells occurs via membrane fusion in late endosomes; however, the mechanism of how the remarkably long virions undergo uncoating, including virion disassembly and nucleocapsid release into the cytosol, remains unknown. Here, we investigate the structural architecture of EBOVs entering host cells and discover that the VP40 matrix disassembles prior to membrane fusion. We reveal that VP40 disassembly is caused by the weakening of VP40–lipid interactions driven by low endosomal pH that equilibrates passively across the viral envelope without a dedicated ion channel. We further show that viral membrane fusion depends on VP40 matrix integrity, and its disassembly reduces the energy barrier for fusion stalk formation. Thus, pH-driven structural remodeling of the VP40 matrix acts as a molecular switch coupling viral matrix uncoating to membrane fusion during EBOV entry.

Introduction

Ebola viruses (EBOVs) are highly pathogenic negative-sense RNA viruses causing severe outbreaks of viral hemorrhagic fever in humans with high case fatality rates (Feldmann & Klenk, 1996).

They enter host cells by macropinocytosis and undergo cytosolic entry in late endosomal compartments, where the fusion of the viral and endosomal membranes leads to genome release into the cytoplasm. EBOVs are characterized by their filamentous morphology, which is determined by the matrix composed of the viral protein 40 (VP40) that drives budding of virions reaching up to several micrometers in length (Geisbert & Jahrling, 1995; Bharat *et al*, 2012). VP40 interacts with negatively charged lipids (Ruigrok *et al*, 2000; Jeevan *et al*, 2016; Johnson *et al*, 2016; Amiar *et al*, 2021) to assemble into a quasi-helical scaffold underneath the viral membrane (Noda *et al*, 2002; Wan *et al*, 2020) and is critical for the incorporation of the viral nucleocapsid into the virions by so far unknown VP40–nucleocapsid interactions. The EBOV nucleocapsid is composed of the nucleoprotein (NP), which encapsidates the single-stranded RNA genome, as well as VP24 and VP35 (Bharat *et al*, 2012; Wan *et al*, 2017; Takamatsu *et al*, 2018). Upon host cell entry, the nucleocapsid needs to dissociate from the virus particle and viral genome to enable genome replication and transcription (Greber *et al*, 1994). These processes together are referred to as virus uncoating, which involves the weakening of protein–protein and protein–membrane interactions inside the virus lumen. The resulting changes in virion architecture allow the timely nucleocapsid release upon membrane fusion (Yamauchi & Greber, 2016). It is well established that fusion of the viral and endosomal membrane relies on interactions with the EBOV fusion glycoprotein (GP), which is the only transmembrane protein that studs the Ebola viral envelope (Dube *et al*, 2009; Lee & Saphire, 2009; Nanbo *et al*, 2010). GP-mediated membrane fusion is triggered after proteolytic processing of GP by host cell cathepsin proteases (Brecher *et al*, 2012) and depends on the interaction of the cleaved GP subunit GP1 with the late endosomal Niemann-Pick C1 (NPC1) receptor (Carette *et al*, 2011; Côté *et al*, 2011; Miller *et al*, 2012; Simmons

1 Schaller Research Groups, Department of Infectious Diseases, Virology, University Hospital Heidelberg, Heidelberg, Germany
2 BioQuant-Center for Quantitative Biology, Heidelberg University, Heidelberg, Germany
3 Institute for Theoretical Physics, Heidelberg University, Heidelberg, Germany
4 Heidelberg University Biochemistry Center, Heidelberg, Germany
5 Department of Physics, University of Helsinki, Helsinki, Finland
6 Department of Infectious Diseases, Integrative Virology, University Hospital Heidelberg, Heidelberg, Germany
7 German Centre for Infection Research (DZIF), Partner Site Heidelberg, Heidelberg, Germany
8 Institute of Molecular Virology and Cell Biology, Friedrich-Loeffler-Insitut, Greifswald-Insel Riems, Greifswald, Germany
   *Corresponding author. Tel: +49 6221 54 51231; E-mail: petr.chlanda@bioquant.uni-heidelberg.de

et al, 2015). However, the molecular mechanism of how the remarkably long EBOV virions undergo uncoating during cytosolic entry remains enigmatic. A growing body of evidence shows that matrix disassembly during viral entry can trigger a cascade of events required for viral uncoating and efficient virus entry (Banerjee *et al*, 2014; Li *et al*, 2014). While the structure of isolated Ebola virions is well characterized, it is currently unknown whether the VP40 matrix undergoes conformational changes during virion entry and factors initiating EBOV disassembly remain to be elucidated. In addition, a mechanistic understanding of how interactions between the EBOV VP40 matrix, the viral membrane, and nucleocapsid are modulated during viral entry is still missing. Since EBOVs is a late-penetrating virus, which requires low endosomal pH for cytosolic entry (Lozach *et al*, 2011), the acidic environment may serve as one of the triggers for virion uncoating.

Here, we investigate EBOV uncoating and the role of VP40 during virus entry into host cells by characterizing EBOVs in endosome-mimicking conditions *in vitro*, and in endo-lysosomal compartments *in situ*, by cryo-electron tomography (cryo-ET), which is complemented by membrane modeling approaches, lipidomics, and time-lapse fluorescence imaging. We find that the VP40 matrix and its interactions with lipids in the viral envelope are sensitive to low pH, which passively equilibrates across the viral envelope in acidic environments. This leads to the disassembly of the matrix layer allowing for fusion and genome release.

Results

The Ebola virus VP40 matrix undergoes disassembly in endosomal compartments

To shed light on endosomal uncoating of EBOV virions at molecular resolution, we infected Huh7 cells cultured on electron microscopy grids with EBOVs (Zaire ebolavirus species, Mayinga strain) in biosafety level 4 (BSL4) containment. Infected cells were chemically fixed using 4% paraformaldehyde (PFA) and 0.1% glutaraldehyde (GA) after multiple rounds of infection had occurred at 48 h post-infection (Fig 1A, at 22 h post-infection: Figs EV1 and EV2, Appendix Figs S1 and S2). After vitrification and cryo-focused ion beam (cryo-FIB) milling of the infected cells, we performed *in situ* cryo-ET of endosomal compartments containing EBOV virions (Fig 1B–G, Movie EV1). Late endosomal compartments were identified by the presence of vesicles and membrane fragments (white arrow, Fig 1F), which are likely products of lysosomal degradation. In addition, we observed the accumulation of crystalline lipidic structures with a spacing of 3.2 nm (Fig EV1), consistent with the spacing found in cholesterol ester crystals previously described in lamellar bodies, lipid droplets, and isolated low-density lipoprotein particles (van Niel *et al*, 2015; Mahamid *et al*, 2019; Klein *et al*, 2020b). Interestingly, Ebola virions in late endosomes retained their filamentous morphology and displayed well-defined nucleocapsids of approximately 20 nm in diameter (Fig 1, Appendix Fig S1). They appeared condensed and resembled nucleocapsid structures formed by truncated EBOV NP alone (Wan *et al*, 2017) but lacked the regular protrusions observed in nucleocapsids of isolated virions (Fig EV2). However, the VP40 matrix layer was detached from the envelope as apparent from the empty space adjacent to the EBOV membrane

and disordered protein densities, which presumably represent disassembled VP40, surrounding the nucleocapsid in the EBOV lumen (Fig 1D–G). Importantly, none of the five EBOV virions captured in endosomes displayed ordered VP40 matrices, and two virions had engulfed intraluminal vesicles (Appendix Fig S1). In contrast, budding virions and extracellular virions adjacent to the plasma membrane of infected cells displayed assembled VP40 layers with VP40 proteins visible as distinct densities lining the membrane (Fig 1H–K, Appendix Fig S2, $n = 8$), similar to the VP40 layer in isolated virions (Fig EV2). We were not able to capture virions residing in endosomes in the process of fusing with the endosomal membrane, presumably because virus membrane fusion is a rapid event. However, in a similar experiment using virus-like particles (VLPs) composed of VP40 and GP, we could confirm the absence of ordered VP40 matrix layers in VLPs inside endosomal compartments. Moreover, we were able to capture one fusion event and several intracellular membranes studded with luminal GPs, indicating that fusion had taken place (Fig EV3). Overall, these data indicate that EBOV uncoating involves VP40 disassembly in late endosomal compartments and suggest that endosomal VP40 disassembly occurs prior to GP-mediated membrane fusion.

Low pH triggers disassembly of the EBOV matrix *in vitro*

We next sought to identify factors driving VP40 disassembly. Since EBOVs enter host cells via late endosomes, which are characterized by low pH, we assessed the effect of external pH on the shape of EBOV VLPs and, in particular, on the structure of the VP40 matrix. VLPs composed of VP40 and GP were produced from HEK 293T cells and analyzed by cryo-ET (Fig 2A–D). At neutral pH, the organization of VP40 proteins into a helical scaffold was apparent from transverse cross-sections as an additional profile adjacent to the inner membrane monolayer and as regular striations spanning the width of the particles when observed close to the VLP surface (Fig 2B and C). Individual VP40 proteins were visible as distinct densities lining the membrane (Fig 2D). To understand their organization within the matrix, we applied subtomogram averaging of the VP40 matrix in purified VLPs. In accord with recently published data (Wan *et al*, 2020), the subtomogram average revealed the linear arrangement of VP40 dimers via their C-terminal domains (CTDs), which are directly connected to the inner membrane monolayer (Fig 2E). The available crystal structure of the VP40 dimer (pdb: 7jzj) fitted well into the average (Fig 2F) except for three short helical segments of one VP40 monomer (Fig EV4A).

To assess whether the VP40 matrix undergoes disassembly at low pH, VLPs were then subjected to the late endosomal pH of 4.5 for 30 min. Consistent with Ebola virions found in late endosomes, the VLPs retained their overall filamentous morphology but did not show ordered VP40 matrix layers. Instead, they contained disordered protein aggregates accumulated at the VLP core (Fig 2G–J). Additionally, a lack of densities between the membrane and protein aggregates indicates that VP40 detaches from the membrane, as particularly apparent from the cross-sections (Fig 2H and J), which was also reflected in a more variable particle diameter (Fig EV4B). To elucidate whether this phenotype depends on the presence of EBOV GP, VLPs composed of VP40 alone were analyzed by cryo-ET. The presence and absence of the ordered VP40 matrix at neutral and low pH, respectively, were clearly apparent as regular striations and
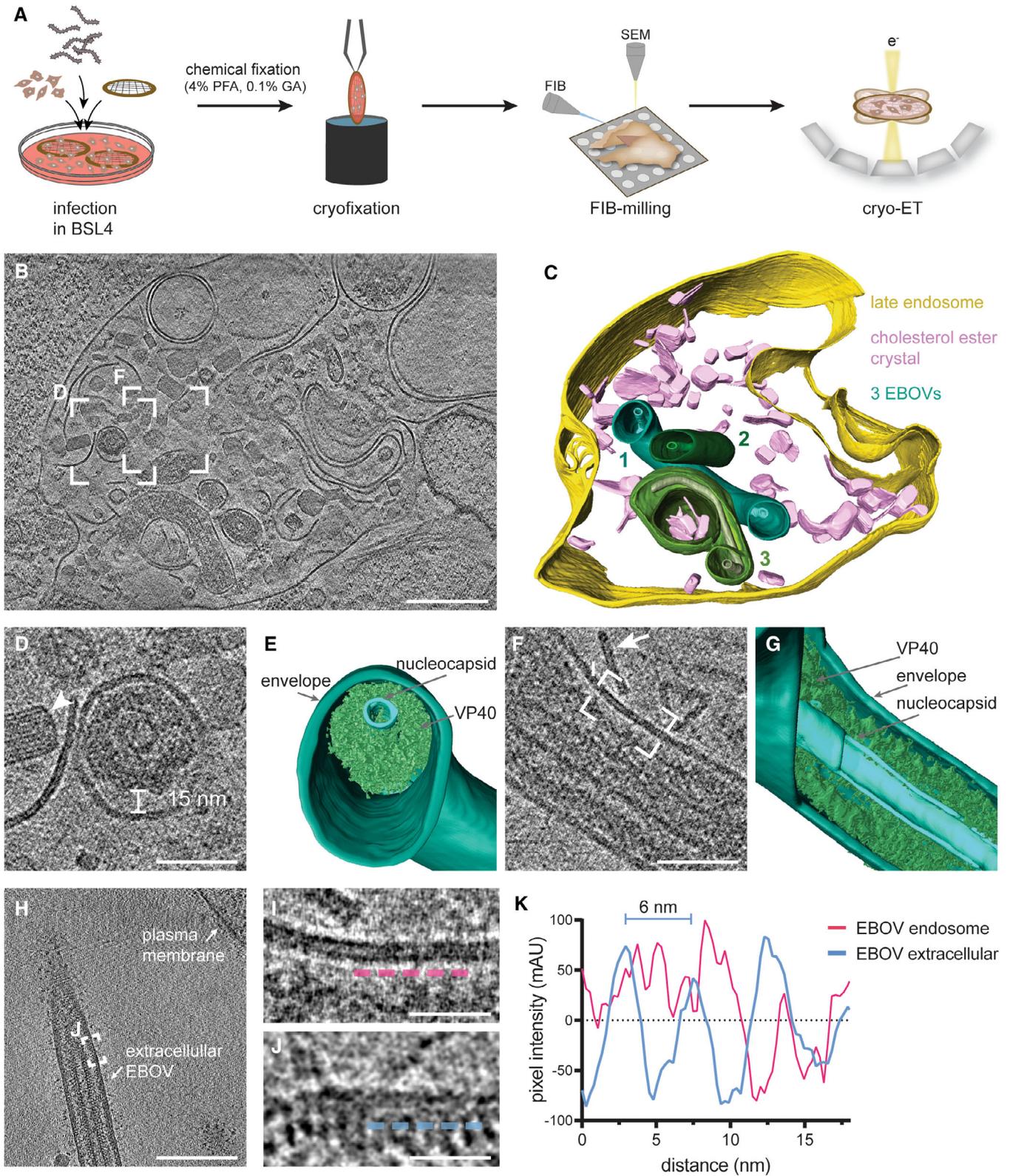
Figure 1.

Figure 1. *In situ* cryo-electron tomography of EBOV virions localized in endosomes of an infected cell.

A   Schematic of the *in situ* cryo-ET workflow, including infection of cells grown on electron microscopy grids and chemical fixation using 4% PFA and 0.1% GA for bio-safety reasons before removal from BSL4. Vitrification was performed prior to cell thinning by cryo-FIB milling and imaging by cryo-ET.
B   Slice through a tomogram showing EBOV virions inside a late endosomal compartment.
C   3D segmentation of the delimiting endosomal membrane (yellow), cholesterol ester crystals (pink), viral membranes (shades of green) of three EBOV virions (numbered 1–3), and nucleocapsids (shades of light green) for visualization.
D   Magnified view of the area highlighted in (B) showing the transverse cross-section of a virion. A cholesterol ester crystal adjacent to the virion is marked by a white arrowhead.
E   3D segmentation of the viral membrane, nucleocapsid, and VP40 shown in (D).
F   Magnified view of a different slice of the tomogram in (B) showing a longitudinal cross-section through a virion. A linear membrane fragment adjacent to the virion is marked with a white arrow.
G   3D segmentation of the viral membrane, nucleocapsid, and VP40 displayed in (F).
H   Slices through a tomogram showing an extracellular EBOV adjacent to the plasma membrane of an infected cell.
I, J   Magnified areas highlighted in (F) and (H), respectively, showing the viral membrane and VP40 densities at the luminal side. For comparison, line profiles at 3 nm distance from the inner membrane monolayer, visualized by dotted profiles (magenta and blue, respectively), were determined.
K   Line profiles adjacent to the inner viral membrane leaflet of a virion inside an endosome and a purified virion before infection.

Data information: Scale bars: (B), (H): 200 nm, (D), (F): 50 nm, (I), (J): 20 nm.
Source data are available online for this figure.

disordered protein accumulations at the particles' cores (Figs 2K and EV4C). Accordingly, line density profiles proximal to the inner membrane monolayer of VLPs showed the 5–6 nm pitch of the assembled VP40 matrix at neutral pH, whereas no repeating densities were detected at low pH (Fig 2L). We further repeated the experiment using VLPs composed of VP40, GP and the nucleocapsid proteins NP, VP24, and VP35, and observed the same low pH-phenotype described above. These results show that nucleocapsid proteins do not influence the VP40 disassembly driven by low pH. Performing the experiments on unpurified VLPs harvested from the supernatant of transfected cells confirmed that the purification protocol applied did not influence the disassembly of the VP40 matrix (Appendix Fig S3). Hence, pH-mediated VP40 disassembly is independent of other viral proteins including the transmembrane protein GP.

VP40 interactions with negatively charged lipids are weakened at low pH

To further probe the specific VP40–lipid interactions at neutral and low pH, we performed all-atom molecular dynamics (MD) simulations and modeled the binding of VP40 dimers to membrane lipids at different pH levels. To this end, we emulated a simplified membrane containing 30% phosphatidylcholine, 40% cholesterol, and 30% phosphatidylserine mimicking the overall negative charge of the VLP inner membrane monolayer. We modeled missing C-terminal residues, which are inherently flexible and disordered, into the VP40 dimer structure (pdb: 7jzj, Wan *et al*, 2020) and simulated VP40–membrane interactions for a cumulative time of 10 μs for each pH using the CHARMM36m force field (Pastor & MacKerell, 2011; Huang & Mackerell, 2013; Huang *et al*, 2016). We show that after one CTD of the VP40 dimer established interactions with phosphatidylserines, the second CTD is pulled toward the membrane, leading to the anchoring of the dimer into the membrane (Fig 3A). The membrane interactions were driven by positively charged residues decorating the C-termini of the VP40 dimer, including K224, K225, K274, and K275, which corroborates experimental data showing that these residues form a basic patch required for membrane association and budding of VLPs (Bornholdt *et al*, 2013). In the MD simulations, the basic patches strongly promote lipid interactions and localize in flexible loops at the CTDs, which penetrate into the inner

membrane monolayer (Fig 3B and C) and correspond to the previously unassigned densities (Wan *et al*, 2020) between the VP40 matrix and viral membrane in the subtomogram average (Fig 2E and F). Moreover, the MD simulations showed that the rotation angle of VP40 monomers oscillates around 1° (SD 9.5) along the N-terminal-dimerization domain and is in agreement with the subtomogram average (Figs 3B and EV5C–E), such that only flexible loops protrude from the average (Fig 3D). Accordingly, when aligning the crystal structure of the VP40 dimer (pdb: 7jzj) with the VP40 structure obtained from the MD simulations, the membrane-proximal loops and short alpha-helices were mismatched while the core of the monomer aligned well (Fig 3B, highlighted in yellow, Fig EV5A and B). The second monomer displayed similar secondary structures, which were tilted with respect to the crystal structure by 17°, causing a mismatch when compared to the crystal structure (Fig 3B, blue monomer, Fig EV5E).

Next, we simulated VP40–membrane interactions at pH 4.5 and observed a significantly decreased affinity toward the membrane, consistent with our tomography data (Fig 3E). The free energy profile determined from the MD simulations (Fig 3E) revealed an energy minimum that was 4.1 k_BT weaker at low pH compared to pH 7.4. However, binding was not completely diminished since 10% of the phosphatidylserines used in the simulation are still charged (Tsui *et al*, 1986), and the membrane modeled here containing high levels of phosphatidylserine can still engage in electrostatic interactions. To identify which lipids are enriched in the VLP membrane and are thus likely involved in VP40 binding, we then determined the VLP lipid composition by mass spectrometry (Figs 3F and EV5, Table EV1). As expected for EBOV VLPs budding from microdomains in the plasma membrane (Panchal *et al*, 2003; Stahelin, 2014), the EBOV VLP envelope was rich in phosphatidylserine and cholesterol, phosphatidylcholine, and sphingomyelin (9, 39, 25, and 9%, respectively). Collectively, these data argue for low pH-mediated VP40 disassembly through neutralization of negatively charged phospholipids in the viral envelope and highlights electrostatic interactions as the main driving forces of the VP40-membrane binding (Fig EV5F). These interactions are driven by basic patches of amino acids, which are highly conserved across all EBOV species (Fig EV5H), further emphasizing their importance in adaptable membrane binding.

Protons passively equilibrate across the EBOV membrane

We next assessed the acidification kinetics to elucidate the mechanism of ion permeability across the viral membrane. EBOV VLPs composed of GP, VP40, and the pH-sensitive GFP variant pHluorin (Miesenböck *et al*, 1998) N-terminally fused to VP40 (pHluorin-

VP40) were prepared to monitor pH changes in VLP lumina upon altering the pH of the surrounding buffer (Fig 4A). Pleomorphic VLPs containing VP40 in excess over VP40-pHluorin, including filamentous and spherical particles, were imaged by time-lapse microscopy (Fig 4B and C). At neutral pH, the VLPs showed a fluorescent signal, which gradually decayed over several minutes after lowering the
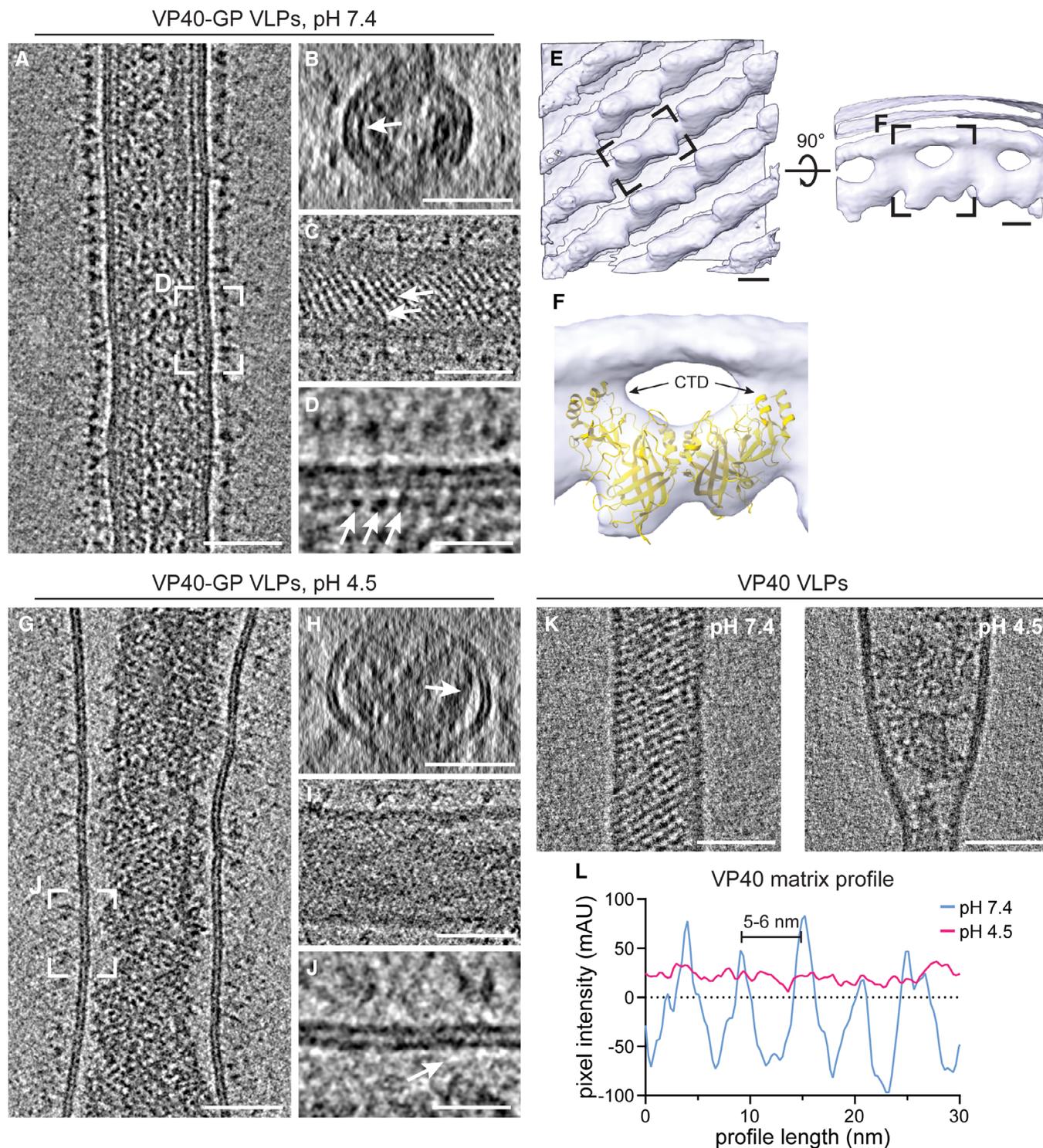
Figure 2.

Figure 2.   The VP40 matrix in EBOV VLPs disassembles at low pH.

A   Slices of a tomogram showing a filamentous EBOV VLP composed of VP40 and GP at neutral pH ($n = 37$).
B, C   Transverse cross-section and longitudinal near-to-surface slices of the tomogram shown in (A) displaying the densities for the outer and inner membrane mono-layer and an additional density of the VP40 matrix apparent as striations in (C) (white arrows).
D   Longitudinal cross-section highlighting the VP40 densities adjacent to the membrane (white arrows).
E   Subtomogram average of the VP40 matrix in EBOV VLPs composed of GP and VP40. A density representing a single VP40 dimer is indicated by a black dashed rectangle.
F   Crystal structure of the VP40 dimer (pdb: 7jzj) fitted into the subtomogram average with the C-terminal domains (CTDs) indicated by arrows.
G–J   Slices of a tomogram showing a filamentous EBOV VLP composed of VP40 and GP after incubation at low pH ($n = 18$). White arrows in (H) and (J) highlight areas adjacent to the VLP membrane devoid of protein densities in contrast to corresponding slices of VLPs at neutral pH.
K   Slices of tomograms showing filamentous VLPs composed of VP40 after incubation at neutral ($n = 22$) and low pH ($n = 8$), respectively.
L   Line density profiles determined adjacent to the inner membrane monolayer of VLPs incubated at neutral (blue) and low pH (magenta). At neutral pH, the VP40 matrix detectable as regular densities in (D) have a 5–6 nm pitch.

Data information: Scale bars: (A–C), (G–I), and (K): 50 nm, (E): 2.5 nm, (D), (J): 20 nm.
Source data are available online for this figure.

external pH (Fig 4D). In contrast, when adding the detergent Triton X-100 (T-X^{100}) before imaging to permeabilize the VLP membrane, the signal decayed to background fluorescence within the first 15 s (Fig 4D), indicating that protonation of pHluorin was slowed down by the membrane of the VLPs. To calculate the acidification kinetics of the VLPs' lumen, we determined pH levels in the VLPs (Fig 4E) by correlating the pHluorin fluorescence intensity to pH using a calibration curve (Appendix Fig S4A). We found that the luminal pH of filamentous VLPs decreased from 7.4 to 6.4 after 6 min, while for the spherical particles, this decay had already occurred after 3.5 min (Fig 4E). We next calculated the membrane proton permeability coefficient, P_m, based on the geometry of the VLPs measured by cryo-ET (Fig 2) and the fluorescence decay times (Appendix Fig S4B). Filamentous VLPs had a permeability coefficient of 1.2 ± 0.2 Å/s, whereas the membrane of spherical VLPs was significantly more permeable with a permeability coefficient of 33 ± 9 Å/s.

To compare the membrane permeability of the VLPs with the permeability of membranes containing a well-characterized viral ion channel, we used HEK 293T cells expressing VP40-pHluorin and the influenza virus ion channel M2. In line with previous measurements (Deamer & Bramhall, 1986; Deamer, 1987), the plasma membrane in cells displayed a permeability coefficient of 345 ± 71 Å/s ($n = 44$) in the absence of M2. As expected, the permeability increased with increasing amounts of M2 present in the plasma membrane up to 1940 ± 562 Å/s ($n = 26$) when M2 and VP40 were transfected at a 1:0.2 molar ratio (Fig 4E and F). Compared to the envelope of filamentous EBOV VLPs, the plasma membrane was more permeable to protons already in the absence of M2.

Disassembly of the VP40 matrix is critical for membrane fusion

Collectively, our experimental data and MD simulations indicate that low pH drives VP40 matrix disassembly and detachment from the viral envelope. We speculated that this influences the GP-mediated membrane fusion between the EBOV envelope and the endosomal membrane. To test this hypothesis, we numerically simulated the membrane fusion pathway in the presence of the VP40 matrix and estimated the magnitude of the two major energy barriers to membrane fusion: stalk and fusion pore formation (Jahn & Grubmüller, 2002; Chernomordik *et al*, 2006; Chernomordik & Kozlov, 2008; Harrison, 2008). We applied a continuum approach to model the lipid membrane with the commonly used framework of

the theory of splay-tilt deformations (Helfrich, 1973; Hamm & Kozlov, 2000) and the VP40 matrix layer as a uniform thin shell that interacts continuously with the virus envelope but can also locally detach from the membrane near the stalk and diaphragm rim (Fig 5A). Based on the VP40-membrane binding energy obtained from the MD simulations at pH 7.4 (Fig 3E) and the density of VP40 dimers on the viral envelope determined from the subtomogram average (Fig 2E), we estimated the VP40 matrix interaction energy density to be 0.38 ± 0.02 k_BT/nm^2 (with a dimer density of 0.036 nm^{-2} and free binding energy of 10.77 ± 0.47 k_BT). Consistently with our cryo-ET data, we assume that the interaction energy density vanishes at low pH due to the VP40 matrix disassembly. Importantly, our calculations showed that the initiation of viral membrane fusion is more favorable after VP40 disassembly. The calculated stalk formation energy barrier drops from 89–79 k_BT to 65 k_BT due to the weakening of the VP40–lipid interactions at low pH, depending on the matrix layer rigidity (Fig 5B). Hence, the intact VP40 matrix can prevent or slow down hemifusion stalk formation, which is the first step of membrane fusion.

Interestingly, our model predicts that fusion pore formation, which occurs after stalk formation, is facilitated in the presence of the assembled VP40 matrix because of increased stress in the hemifusion diaphragm. Simulation data showed that the interaction energy density and the rigidity of the VP40 matrix modulate the shape of the hemifusion diaphragm structure (Fig 5C), which determines the energy barrier of pore formation. Strong interactions between the lipids and VP40 matrix (Fig 5C, "tight-bound" configuration) stabilize the hemifusion diaphragm, thereby inhibiting fusion pore formation. Conversely, in case of a weakly interacting or stiff VP40 matrix (Fig 5C, "loose" configuration), the hemifusion diaphragm is more unstable, which results in a lower energy barrier for fusion pore formation (Fig 5D). Our model showed that the minimal pore opening energy is at the phase boundary between "loose" and "tight-bound" configurations, where diaphragm stress is maximal (Fig 5D). Given the VP40-membrane binding energy and VP40 dimer envelope density found in the MD simulations (Fig 3E), we could show that the VP40 matrix and the membrane preferably adopt the "loose" configuration at both neutral and acidic pH. Therefore, contrary to the stalk formation energy barrier, which is decreased upon VP40 matrix disassembly, the pore formation energy barrier is lower in the presence of the VP40 matrix layer by 16–33 k_BT (Fig 5D), depending on the matrix layer rigidity (Fig 5E,
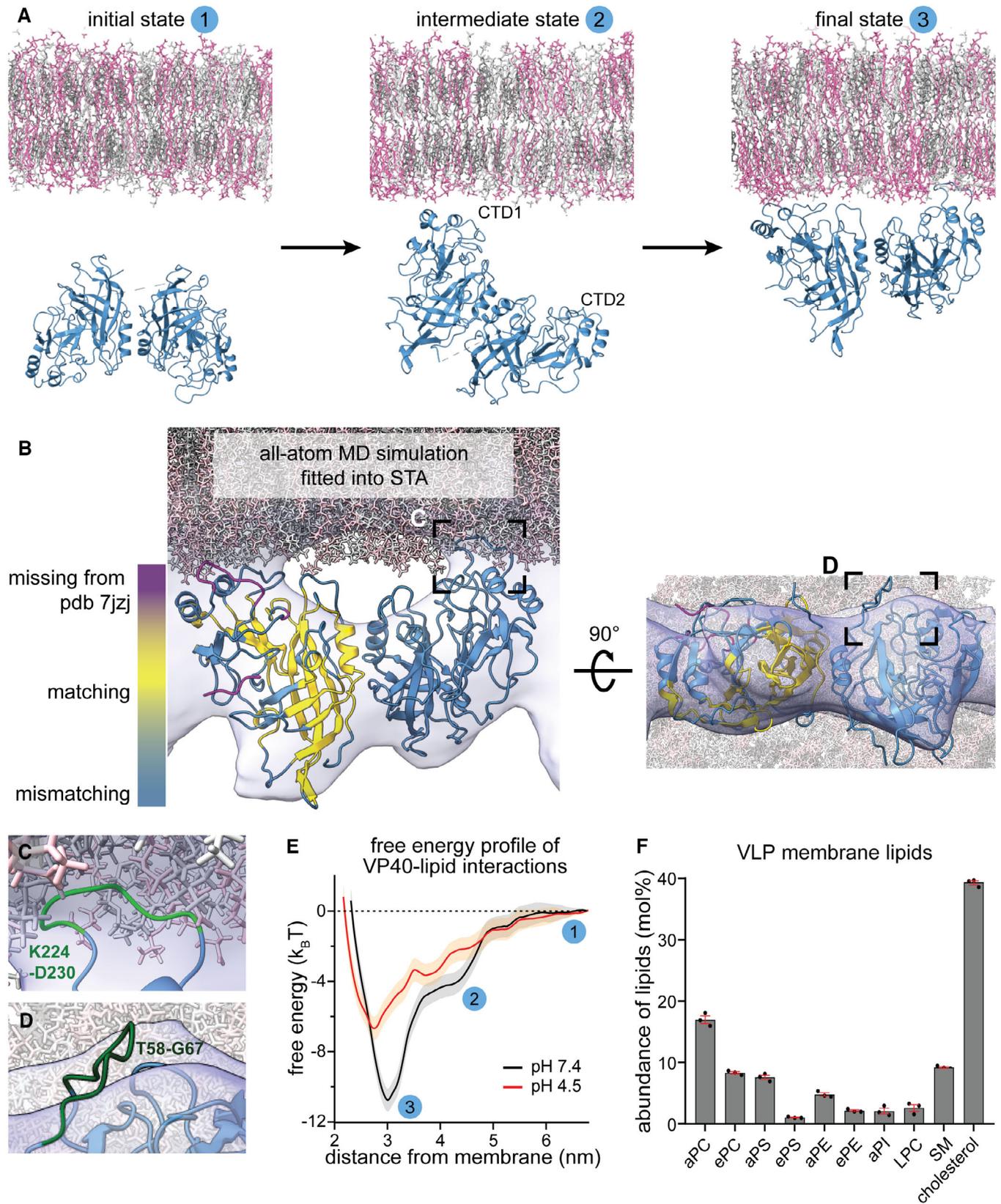
Figure 3.

◀

Figure 3. VP40–lipid interactions at neutral and low pH.

A   Initial, intermediate, and final state of the VP40-membrane interaction pathway sampled with unbiased all-atom molecular dynamics (MD) simulations. The simulated membrane is composed of 30% phosphatidylcholine, 40% cholesterol, and 30% phosphatidylserine. VP40 is randomly oriented towards the membrane in the initial state. Lipid interactions are first mediated via one C-terminal domain (CTD1) (intermediate state) before the second CTD (CTD2) is ultimately pulled towards to membrane.

B   MD simulation frame of the VP40-membrane-bound state, with a rotation angle of VP40 monomers along the N-terminal-dimerization domain (Appendix Fig S1C and D) of 1°, fitted into the subtomogram average shown in (Fig 2E). Missing C-terminal residues in the crystal structure of the VP40 dimer (pdb: 7jzj) were computationally modeled (magenta). VP40 conformational changes upon lipid-interaction resulted in a displacement of secondary structures (steel blue), while the core of the protein remained unaltered in comparison to the crystal structure (yellow).

C   The area highlighted in (B) shows a flexible, C-terminal loop (green) containing the residues K224 and K225 that interact with phosphatidylserines in the inner membrane monolayer.

D   Area highlighted in the rotated MD simulation in (B) showing a flexible loop (residues T58-G67) protruding from the subtomogram average.

E   Free energy profiles of VP40–lipid interactions at pH 7.4 and pH 4.5 determined from MD simulations. The plot shows free energy (in k_BT) at increasing membrane-VP40 distances (nm) with indicated three states shown in (A).

F   EBOV VLP lipid composition showing highly abundant lipids determined by mass spectrometry in mol%. Lipid abbreviations: phosphatidylcholine (PC), phosphatidylserine (PS), phosphatidylethanolamine (PE), phosphatidylinositol (PI), lyso-phosphatidylcholine (LPC), sphingomyelin (SM). Prefix "a" indicates acyl-linked glycerophospholipids, prefix "e" indicates ether-linked (plasmanyl) or the presence of one odd and one even chain fatty acyl. Bars represent mean and error bars represent standard error of the mean (red); $n = 3$ biological replicates.

Source data are available online for this figure.

Appendix Fig S5A). However, it is important to note that hemifusion precedes pore formation in the membrane fusion pathway. Since the disassembly of the VP40 matrix is required for hemifusion and hence for the initiation of membrane fusion, it determines the outcome of the membrane fusion pathway.

To validate this theoretical model experimentally, we performed beta-lactamase entry assays using VLPs (Jones & Padilla-Parra, 2016). EBOV membrane fusion requires proteolytic cleavage of GP by low pH-activated cathepsin proteases (Brecher *et al*, 2012) and subsequent binding of the cleaved GP1 subunit to the endosomal receptor NPC1. To circumvent the need for low pH to activate cathepsin proteases, we substituted cathepsins with thermolysins which are active at neutral pH (Stauffer, 1971), thereby decoupling the low pH requirement from proteolytic GP processing. EBOV VLPs composed of GP, VP40, and beta-lactamase N-terminally fused to VP40 (BlaM-VP40) were purified and subjected to thermolysin treatment followed by incubation at neutral or low pH. We then incubated target Huh7 cells with the pretreated VLPs, loaded the cells with a fluorescent BlaM substrate, and assessed virus entry by FACS (Appendix Fig S5). Thermolysin treatment significantly enhanced host cell entry, whereas the enhancement of entry by low pH treatment alone was less pronounced and not statistically significant (Fig 5F). To determine whether thermolysin-treated VLPs still require low pH for entry, we challenged host cells treated with ammonium chloride, which blocks endosomal acidification. Strikingly, entry of VLPs treated with thermolysin was completely inhibited by ammonium chloride, which is in line with a previous study conducted with bafilomycin to inhibit endosomal acidification (Mingo *et al*, 2015b). This suggests that GP processing alone is insufficient to enable entry. Conversely, low pH treated VLPs were also unable to enter target cells treated with ammonium chloride since impaired endosomal acidification prevents the activation of cathepsin proteases and hence GP priming. Combined thermolysin- and low pH-treatment of VLPs *in vitro* rescued entry into host cells with inhibited endosomal acidification, albeit to a lesser extent compared to entry into untreated cells. Since thermolysin-treated EBOV VLPs efficiently enter untreated host cells at neutral and low pH, we further conclude that low pH alone does not induce

the GP2 post-fusion conformation, which would inhibit virus entry. Together, this suggests a role of low endosomal pH beyond proteolytic processing of EBOV GP, likely for the disassembly of the VP40 matrix. Overall, these data show that VP40 matrix integrity modulates GP-mediated membrane fusion, strongly supporting the notion that VP40 disassembly is required for and precedes membrane fusion.

Discussion

Ebola viruses form remarkably long, filamentous virions that enter the cytoplasm by fusion with late endosomal membranes. Similar to other enveloped viruses, the shape and stability of EBOVs are determined by a matrix layer forming a flexible scaffold underneath the viral envelope, which is indispensable for particle formation and protects the encapsidated genome during transmission. Here, we investigate the molecular architecture of the EBOV VP40 matrix in Ebola virions during host cell entry to elucidate whether and how it is released from the viral envelope to allow virion uncoating. Using *in situ* cryo-electron tomography, we directly visualize EBOVs entering host cells via the endosomal route. Virions inside endosomal compartments exclusively exhibited disassembled VP40 matrices and some had engulfed endosomal vesicles, suggesting that the membranes of these virions are sufficiently flexible to engage in membrane fusion (Fig 1). Considering that the nucleocapsids in all endosomal EBOVs were condensed, we propose that VP40 disassembly precedes membrane fusion, while nucleocapsid integrity is maintained until cytoplasmic entry is concluded. The VP40 aggregation surrounding the nucleocapsid may be involved in engaging cellular factors required to pull nucleocapsids out of the fusion site as has recently been suggested for influenza A virus, whose disassembled M1 matrix layer recruits the aggresome machinery by mimicking misfolded proteins (Banerjee *et al*, 2014). Supported by our functional data and computational simulations, we propose that EBOV uncoating occurs in a cascade-like fashion. Tightly regulated by pH, uncoating starts with the disassembly of the VP40 layer, followed by GP-driven membrane fusion and release of the compact nucleocapsid into the
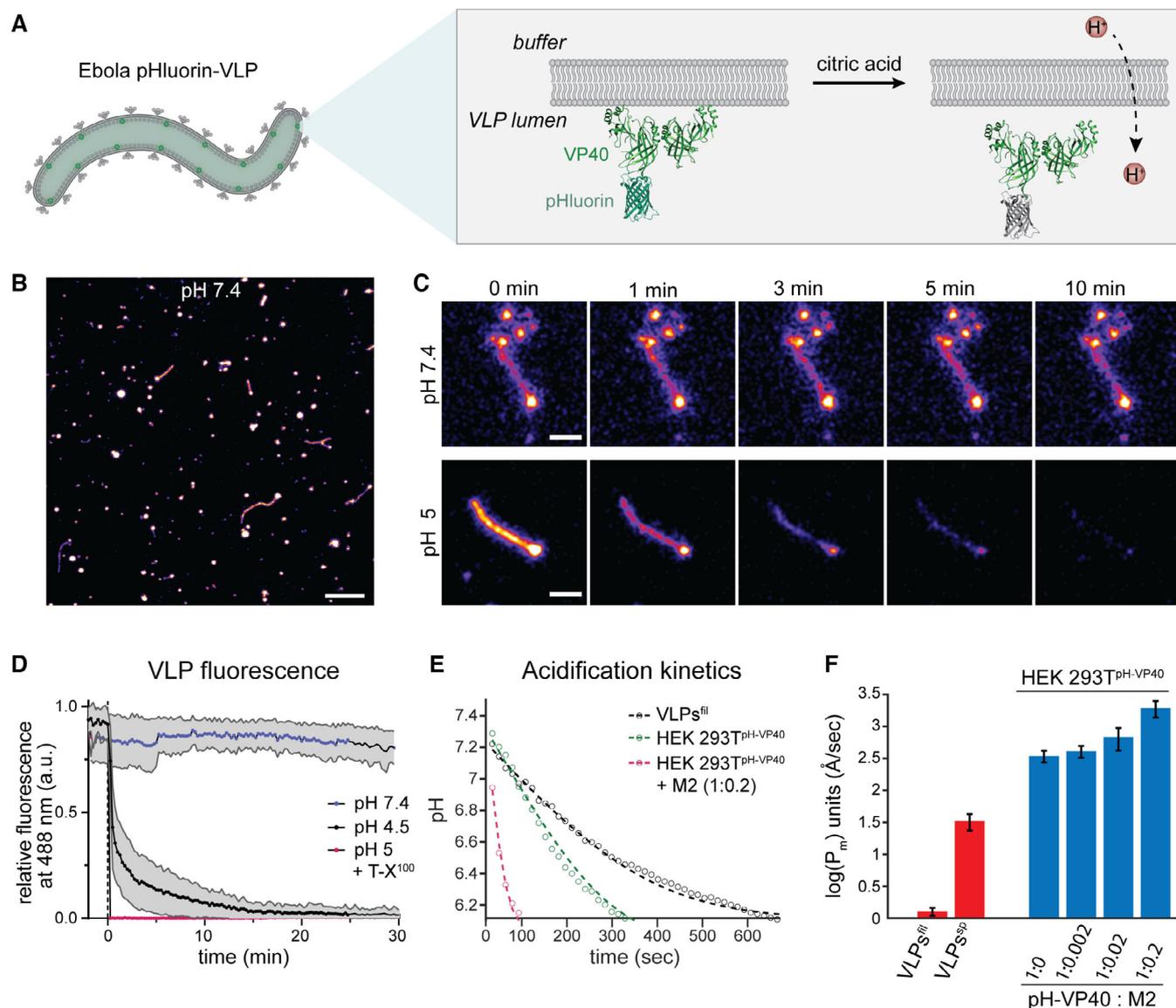
Figure 4. Time-lapse microscopy of EBOV VLPs at different pH.

A Schematic showing the VLP membrane and pHluorin-VP40 facing the luminal side of the VLPs. Upon protonation, pHluorin loses its fluorescence properties and serves as a proxy for proton diffusion across the membrane.

B Overview confocal fluorescence microscopy image showing pleomorphic pHluorin-labeled VLPs composed of VP40, pHluorin-VP40 (ratio 10:1) and GP.

C Magnified images of representative VLPs acquired during time-lapse microscopy at neutral pH and after acidification to approximately pH 5. Frames are exemplarily shown at 0, 1, 3, 5 and 10 min after lowering the external pH.

D Plot showing the mean relative fluorescence intensities and standard deviation of VLPs imaged at neutral pH, low pH and in the presence of T-X^{100} at low pH over time. Data was obtained from 3 independent VLP preparations. Number of technical replicates: $n = 42$ (pH 7.4); $n = 19$ (pH 4.5 and pH 5 + T-X^{100}).

E Plot showing the drop of pH inside VLPs over time after lowering the pH of the surrounding buffer to 5. The dots represent the mean values, and the dashed lines are the theoretical fit to Equation 3.

F Membrane permeability of VLPs (red) and HEK 293T cells expressing different ratios of VP40 and M2 (blue). The mean permeability obtained from 3 independent VLP preparations and 3 biological replicates of cell transfections is displayed on a logarithmic scale, error bars represent standard errors of the mean. Permeability coefficients: filamentous VLPs 1.2 ± 0.2 Å/s ($n = 154$), spherical VLPs 33 ± 9 Å/s ($n = 66$), cells expressing no M2 345 ± 71 Å/s ($n = 44$), cells expressing pHluorin-VP40 and M2 at 1:0.002 molar ratio 409 ± 85 Å/s ($n = 30$), cells expressing pHluorin-VP40 and M2 at 1:0.02 molar ratio 683 ± 263 Å/s ($n = 28$) and cells expressing pHluorin-VP40 and M2 at 1:0.2 molar ratio 1940 ± 562 Å/s ($n = 26$).

Data information: Scale bars: B: 10 µm, C: 2 µm.
Source data are available online for this figure.

cytoplasm. It remains to be elucidated when and how the nucleocapsid undergoes de-condensation to allow viral genome replication and transcription.

The organization of VP40 proteins within the VP40 matrix, including their oligomeric state and orientation of C-termini towards the membrane, has long been subject of debate (Scianimanico

et al, 2000; Adu-Gyamfi et al, 2013; Soni & Stahelin, 2014; Stahelin, 2014; Del Vecchio et al, 2018; Pavadai et al, 2018). While the structure of VP40 in solution was revealed as a dimer (Bornholdt

et al, 2013), structures of VP40 in the context of lipid environments were proposed based on purified VP40 proteins either truncated or characterized in the presence of lipid mimics. These revealed VP40
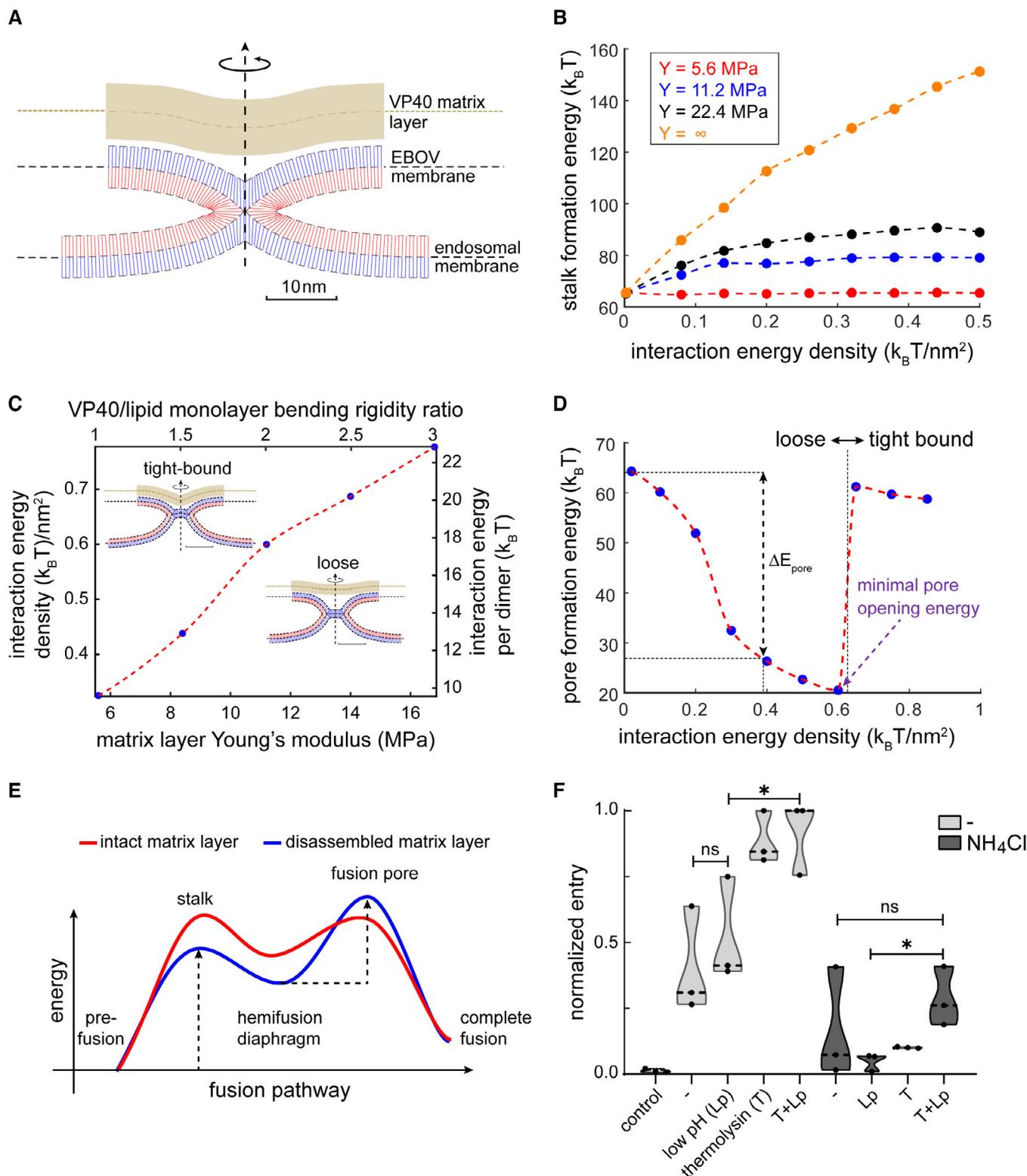
Figure 5.

◀

Figure 5. Membrane fusion dynamics in the presence and absence of the VP40 layer.

A   Simulation result of a hemifusion stalk in the presence of a rigid matrix layer (VP40). The blue and red lines represent the averaged lipid director of the distal and proximal monolayers, respectively. The VP40 matrix layer is represented by the continuous thick brown strip. Parameters used in panels (A–D) for the lipid membrane: lipid monolayer bending rigidity 10 k_BT, tilt decay length 1.5 nm, saddle splay modulus to bending modulus ratio -5 k_BT, monolayer spontaneous curvature -0.22 nm^{-1}, and monolayer width 1.5 nm. VP40 matrix layer: width 4 nm, Poisson's ratio 0.5, and membrane mid-plane to VP40 mid-plane optimal distance 4 nm. In panel (A) the matrix layer Young's modulus is 11.2 MPa, and the interaction energy density is 0.2 k_BT/nm^2.

B   Stalk formation energy as a function of VP40-membrane interaction energy. The stalk energy for non-interacting VP40 matrix ($u_0 = 0$) is 65 k_BT. VP40 matrix layer Young's modulus legend – red 5.6 MPa, blue 11.2 MPa, black 16.8 MPa, and orange is infinitely rigid. The bending rigidity ratio between the VP40 matrix layer and lipid monolayer are 1, 2, 3, and infinity, respectively. The line represents an infinitely rigid layer.

C   Hemifusion diaphragm configurations phase-diagram – above dotted red line: tight-bound solution and loose configuration below. The inserts are simulation results with layer Young's modulus of 11.2 MPa. The interaction energy density is 0.2 k_BT/nm^2 in loose configuration and 0.85 k_BT/nm^2 in the tight-bound configuration. The scale bar is 10 nm.

D   Fusion pore formation energy as a function of VP40-membrane interaction energy. The discontinuity in the energy is located at the phase line between configurations (see C). The change in pore formation energy, ΔE_{pore} is defined as the difference between fusion-pore formation energy at interaction energy density 0.2 k_BT/nm^2 (the value found using MD simulations) to the matrix-free case (no interaction energy). (A–D) Dotted lines serve as a guide to the eye.

E   Illustration of the effect of the matrix layer on the fusion pathway and the fusion intermediates in the absence of the matrix layer. As a result of the presence of the matrix layer, the stalk formation energy barrier increases while the pore formation energy barrier decreases and the hemifusion diaphragm intermediate is less stable.

F   Quantification of FACS data showing EBOV VLP entry as measured by a fluorescence shift of infected cells from emission at 510 nm (no entry) to 450 nm (entry). VLPs were treated prior to infection as indicated on the x-axis, with control: uninfected control cells, −: no treatment, T: thermolysin-treatment at neutral pH, Lp: low pH treatment. Target cells were treated with media or ammonium chloride (NH_4Cl), $n = 3$ with 10,000 cells measured per sample.

Source data are available online for this figure.

hexamers as the building blocks of the VP40 matrix (Scianimanico *et al*, 2000; Nguyen *et al*, 2005; Bornholdt *et al*, 2013), in which the C-termini alternately face the viral membrane. Recently published data (Wan *et al*, 2020) and our subtomogram averaging (Fig 2) show that the VP40 matrix within VLPs is instead composed of linearly arranged dimers, in which all C-termini are facing the VLP membrane and thus collectively contribute to the electrostatic interactions. Importantly, a combination of MD simulations and subtomogram averaging allowed us to refine the structure of the VP40 dimer interacting with the membrane and to map the basic patch of lysine residues to flexible loops that extend into the inner membrane monolayer (Jeevan *et al*, 2017; Fig 3). Additionally, our MD simulations reveal lipid-induced conformational changes of the VP40 dimer that complement our subtomogram averaging data. The rotation of VP40 monomers along the N-terminal-dimerization domain is in line with the structural data and emphasizes the modularity of the VP40 dimer, which may contribute to the flexibility of the large filamentous particles (Booth *et al*, 2013; Wan *et al*, 2020).

Using VLPs of minimal protein composition (VP40 and GP and VP40 alone), we show that VP40-disassembly, i.e. the detachment of the matrix from the viral envelope is triggered by low endosomal pH (Fig 2). This indicates that VP40 disassembly does not depend on structural changes of other viral proteins, including GP, and is driven solely by the acidic environment. Furthermore, we deduced VP40–lipid interaction strengths from the MD simulations, which are strongly diminished at pH 4.5 and thus support a dissociation of VP40 from the membrane in endosomal environments. Our data demonstrate that VP40 detachment from the membrane is driven by the neutralization of negatively charged phospholipids at endosomal pH. VP40 detachment from viral envelope is caused by a disruption of electrostatic interactions between VP40 and negatively charged lipids in the viral envelope, which have experimentally been demonstrated and attributed to a basic patch of lysine residues decorating the VP40 C-termini (Ruigrok *et al*, 2000; Bornholdt *et al*, 2013; Del Vecchio *et al*, 2018; Lee *et al*, 2021). Considering that matrix protein assembly of other RNA viruses relies on electrostatic interactions

with negatively charged lipids (Norris *et al*, 2022), we propose that pH-mediated matrix disassembly is a general mechanism critical for viral uncoating.

Notably, pH-driven structural remodeling of viruses has so far only been shown and extensively studied for influenza A virus (Fontana & Steven, 2013), which is known to encode the viral ion channel M2 (reviewed here (Manzoor *et al*, 2017)). Since EBOVs do not encode a dedicated ion channel, we determined the permeability of the EBOV VLP membrane in comparison to the plasma membrane in the absence and presence of the M2 ion channel. We show that the proton permeability of the VLP membrane depends on particle morphology and is markedly lower in filamentous VLPs when compared to spherical VLPs (Fig 4). Since spherical EBOV virions are predominantly released at very late infection time-points (4 days post infection) and are less infectious than filamentous particles (Welsch *et al*, 2010), it is plausible that their membrane properties including proton permeability result from improper particle formation due to cell exhaustion. The higher proton permeability of the plasma membrane already in the absence of M2 likely results from its complex composition comprising host cell ion channels (DeCoursey, 2008). While the membrane permeability of filamentous VLPs is low compared to values reported in the literature for protein-free liposomes (Deamer & Bramhall, 1986), pH equilibration inside filamentous virions is fast due to their small radius and takes place within minutes. This suggests that acidification occurs rapidly after EBOV uptake into late endosomes and is not rate-limiting during virus entry into host cells, in agreement with a previous report (Mingo *et al*, 2015a). Taken together, we show that protons diffuse passively across the EBOV envelope, independent of a dedicated ion channel. It remains to be elucidated whether virion acidification also occurs by passive diffusion in other late-penetrating viruses lacking a dedicated ion channel.

We further show that the energy barriers of both the hemifusion stalk and fusion pore formation strongly depend on the VP40 matrix rigidity (Fig 5). The assembled VP40 matrix inhibits stalk formation, which precedes fusion pore formation during membrane fusion,

arguing for VP40 disassembly as a critical step required for membrane fusion and highlighting the role of the matrix as a modulator of membrane fusion. Together, the findings presented here reveal a yet unknown role of viral matrix proteins during viral entry and uncoating as membrane fusion modulators. We propose that low-pH-driven matrix protein disassembly is decisive for membrane fusion of other enveloped late-penetrating viruses, making the process a promising target for interventions by development of virus matrix-specific weak base inhibitors.

Materials and Methods

Cell lines and EBOV VLP production

Cell lines used in this work include HEK 293T cells for Ebola virus-like particle (VLP) production and Huh7 cells as target cells to assess VLP and EBOV entry. HEK293T (293T ECACC, 1202201) cells were purchased from Sigma-Aldrich. Huh7 cells were kindly provided by Prof. Ralf Bartenschlager (Heidelberg University Hospital). Both cell lines were maintained in DMEM media (ThermoFisher Scientific) supplemented with 10% (v/v) FBS and 100 U/ml penicillin–streptomycin (ThermoFisher Scientific) at 37°C, 5% CO_2. All cells were tested for Mycoplasma contamination every 3 months.

Ebola virus VLPs were produced by transfecting HEK 293T cells with equal amounts of pCAGGS plasmids encoding EBOV GP, VP40, NP, VP35, and VP24 (species *Zaire ebolavirus*, Mayinga strain). Supernatants of transfected cells were harvested 48 h post transfection and clarified by centrifugation at 398 *g* for 10 min and 2,168 *g* for 15 min (JA-10 rotor, Beckmann). Clarified supernatants were passed through a 30% sucrose cushion in HNE buffer (10 mM HEPES, 100 mM NaCl, 1 mM EDTA, pH 7.4) by centrifugation for 2.5 h at 15,960 *g* (SW32 Ti rotor, Optima L-90 K ultracentrifuge, Beckmann) at 4°C. Pellets were resuspended in HNE buffer and centrifuged at 12,817 *g* (TLA 120.2 rotor, Optima TLX ultracentrifuge (Beckmann)) at 4°C for 10 min to remove residual media and sucrose. Final pellets were resuspended in HNE buffer and protein concentrations were measured using the Pierce BCA Protein Assay Kit (ThermoFisher Scientific) according to the manual provided by the manufacturer.

To produce reporter VLPs, pHluorin was N-terminally cloned to VP40 and beta-lactamase-VP40 (BlaM-VP40) was a kind gift from Dr. Kartik Chandran. Reporter VLPs were produced by transfecting EBOV GP, VP40, and pHluorin-VP40 or BlaM-VP40 in a 10:10:1 ratio and purified as described above.

Production of Ebola virus and infection of Huh7 cells

Ebola virus (species *Zaire ebolavirus*, strain Mayinga) was produced in VeroE6 cells in the BSL4 facility at the Friedrich-Loeffler Institut (Insel Riems, Greifswald), following approved standard operating procedures. 5 days post-infection, supernatants of infected cells were harvested and purified as described for the VLPs above and then fixed by adding paraformaldehyde and glutaraldehyde in HNE buffer for a final concentration of 4% and 0.1%, respectively.

For structural characterization of EBOV-infected cells, Huh7 cells were seeded on 200 mesh Au Quantifoil™ SiO_2 R1.2/20 EM grids placed on 3D-printed grid holders in a 96-well plate (Fäßler *et al*, 2020). 0.0075×10^6 cells were seeded and the plates were

transferred to the BSL4 laboratory after 4–5 h. Cells were infected with unpurified EBOVs at an MOI of 0.1 for either 22 h or 48 h before chemical fixation for 24 h with 4% paraformaldehyde and 0.1% glutaraldehyde in PHEM buffer (60 mM PIPES, 25 mM HEPES, 2 mM $MgCl_2$, 10 mM EGTA, pH 6.9). After transfer of the samples out of BSL4, the grids were kept in PHEM buffer and plunge-frozen within three days.

Sample preparation for cryo-electron tomography

Ebola virus VLPs and chemically fixed EBOV were plunge-frozen as previously described (Winter & Chlanda, 2021). Briefly, VLPs were diluted to approximately 10–20 ng/µl, mixed with 10 nm protein A-coated colloidal gold (Aurion), and applied onto glow-discharged EM grids (200 mesh, R 2/1, Quantifoil) prior to plunge-freezing with a Leica EM GP2 automatic plunge-freezer.

Chemically fixed EBOV-infected Huh7 cells on EM grids were vitrified using the GP2 plunge freezer (Leica) at an ethane temperature of −183°C, chamber temperature of 25°C, and 95% humidity. 5 µl PHEM buffer was added to the grids before blotting them from the back with a Whatman Type 1 paper for 3 s. For cryo-FIB milling, the grids were clipped into specifically designed AutoGrids™ (Thermo-Fisher Scientific).

Cryo-FIB milling was performed as previously described (Klein *et al*, 2020b) using an Aquilos dual-beam FIB-SEM microscope (ThermoFisher Scientific). Briefly, cells were selected for milling and coated with an organometallic platinum layer for 5 s before milling in four successive steps using a gallium-ion beam at acceleration voltage 30 eV. Resulting lamellae were 200–250 nm thick.

Tomogram acquisition, reconstruction, and volume rendering

Cryo-ET of VLPs and lamellae of EBOV-infected Huh7 cells were performed as previously described (Klein *et al*, 2020a). Briefly, data were collected on a Titan Krios Transmission Electron Microscope (TEM, ThermoFisher Scientific) at Heidelberg University operated at 300 keV and equipped with a BioQuantum® LS energy filter with a slit width of 20 eV and K3 direct electron detector (Gatan). Tilt series were acquired at 33,000 magnification (pixel size 2.671 Å) using a dose-symmetric acquisition scheme (Hagen *et al*, 2017) with an electron dose of approximately 3 e⁻/Å² per projection with tilt ranges from 60° to −60° in 3° increments using SerialEM (Mastronarde, 2005) and a scripted dose-symmetric tilt-scheme (Hagen *et al*, 2017).

For subtomogram averaging, tomograms were acquired at EMBL Heidelberg using a Titan Krios TEM (ThermoFisher Scientific) operated at 300 keV and equipped with a Gatan Quantum 967 LS energy filter with a slit width of 20 eV and a Gatan K2xp detector. Tilt series were acquired at 81,000 magnification (pixel size 1.7005 Å) at a defocus range of −3 to −1.5 µm using SerialEM (Mastronarde, 2005) and a scripted dose-symmetric tilt scheme (Hagen *et al*, 2017) from −60° to 60° with 3° steps.

Tomograms were reconstructed using the IMOD software package (Mastronarde & Held, 2017). Stacks of tomograms of VLPs were aligned using gold fiducials, and stacks of tomograms acquired on lamellae were aligned using patch tracking. After 3D contrast transfer function (CTF) correction and dose filtration implemented in IMOD, the reconstruction was performed by weighted back-projections with a simultaneous iterative reconstruction technique

(SIRT)-like filter equivalent to 10 iterations. Tomograms used for subtomogram averaging were reconstructed using 2D CTF correction by phase flipping and weighted back-projection without a SIRT-like filter. For visualization, 10 slices of the final tomogram were averaged and low-pass filtered.

3D segmentation was performed using the Amira software and the implemented membrane enhancement filter. Membranes were automatically segmented using the Top-hat tool, and final segmentations were manually refined.

Subtomogram averaging

Subtomogram averaging of the VP40 matrix was performed using the Dynamo software package (Castaño-Dıez et al, 2012; Castaño-Dıez, 2017). Particles were automatically picked using the filament model, and subtomograms were extracted with a cubic side length of 128 voxels from 23 tomograms. A reference template was obtained by iteratively aligning and averaging of 50 subtomograms using a mask permitting alignments only a membrane VP40 layer. The initial average was then used as a template for the final averaging of approximately 7,800 particles.

Molecular dynamics simulations

We used the truncated (residues 45–311) crystallographic structure of the VP40 dimer deposited by Norris et al (2022) (pdb: 7JZJ; Wan et al, 2020) for atomistic molecular dynamics simulations. The missing CTD loops were modeled using the GalxyFill software (Coutsias et al, 2004) within the CHARMM-GUI web server (Jo et al, 2008). The protonation states of the proteins at pH 7.4 and 4.5 were calculated through the PROPKA web server (Søndergaard et al, 2011), which indicated a change in the protonation state at pH 4.5 for the following residues: E76, E325, H61, H124, H210, H269, and H315. Importantly, these residues are located away from the interaction interface of VP40 with the membrane and their protonation accordingly does not influence membrane binding. However, protonation of these residues may contribute to conformational changes that facilitate the VP40 disassembly. First, the proteins were simulated in water with a 0.1 M NaCl for 1 μs. Next, the final structures were placed at a distance of 2 nm from a previously built model membrane surface containing POPC:POPS:CHOL (30:30:40) at 10 different random orientations. The model membrane was made using the CHARMM-GUI membrane builder (Jo et al, 2009). Since the percentage of POPS charged molecules at pH 4.5 is 10% (Tsui et al, 1986), we modeled the membrane at pH 4.5 by randomly replacing 90% of POPS molecules with its protonated model (POPSH). Then, each of the 10 repeats was solvated with 40,913 water molecules and 0.1 M NaCl. Next, charges were neutralized by adding or removing the needed amount of Na^+- or CL^--ions. Finally, each system was simulated for 1 μs under NpT conditions. Four out of 10 simulations, at both pH conditions, showed VP40 dimer binding to the membrane with the experimentally known binding residues, K224, K225, K274, and K275. These simulations were used for the analysis. For the production run, we employed the Parrinello-Rahman barostat (Parrinello & Rahman, 1981) with a semi-isotropic pressure coupling scheme and a time constant set to 5.0 ps to maintain the pressure constant. The pressure was set to 1.0 bar and the isothermal compressibility to $4.5 \times 10^{-5} bar^{-1}$. The temperature was maintained at

310 K using the Nose-Hoover thermostat (Hoover, 1985) with a time constant of 1.0 ps. Electrostatic interactions were handled using the PME method (Essmann et al, 1995). The cutoff length of 1.2 nm was used for electrostatic (real space component) and van der Waals interactions. Hydrogen bonds were constrained using the LINCS algorithm (Hess et al, 1997). Finally, periodic boundary conditions were applied in all directions. The simulations were carried out using an integration time step of 2 fs with coordinates saved every 100 ps. All simulations have been carried out with the GROMACS-2021 software (Abraham et al, 2015). Protein, lipids, and salt ions were described using the CHARMM36m force field (Pastor & MacKerell, 2011; Huang & Mackerell, 2013; Huang et al, 2016). For water, we used the TIP3 model (Jorgensen et al, 1983). All pictures, snapshots, and movies were rendered with the visual molecular dynamics (VMD) software (Humphrey et al, 1996).

Free energy calculation

The potential of mean force (PMF) for the VP40 dimer binding on a model membrane surface was calculated using an atomistic resolution, employing the umbrella sampling protocol (Torrie & Valleau, 1974, 1977). The initial configuration for each umbrella window was taken directly from unbiased MD simulations. The center of the mass distance between the VP40 dimer and the phosphate atoms of one leaflet was used as the reaction coordinate. A total of 49 windows, 0.1 nm spaced, were generated and simulated with a harmonic restraint force constant of 2,000 kJ/mol/nm² for 200 ns. The first 100 ns of the simulations were considered as an equilibration phase and discarded from the actual free energy calculation. The free energy profiles were reconstructed using the weighted histogram analysis method (Hub et al, 2010). The statistical error was estimated with 200 bootstrap analyses.

Dihedral angle calculation

The rotation angle of VP40 monomers along the NTD-dimerization domain is defined as the angle between the plane containing the vector connecting alpha carbon atoms of L75^{monomer1} and T112^{monomer1} and the vector connecting atoms T112^{monomer1} and T112^{monomer2} and the plane containing this second vector and the vector connecting atoms T112^{monomer2} and L75^{monomer2} as explained in Fig EV5C. The angle has been calculated rerunning the simulations trajectory with a GROMACS version patched with the open-source, community-developed PLUMED library (Bonomi et al, 2019), version 2.4 (Tribello et al, 2014). The angle measurement in water has been calculated using all simulation frames. For the angle calculation upon the binding to the membrane, the last 100 ns of the four simulations showing VP40-membrane interaction via the experimentally known critical residues (i.e., K224, K225, K274, and K275) have been used.

Regardless of pH, VP40 monomers within the dimer are flexible with a rotation angle, defined as the torsional angle around the alpha carbons of residue T112 of the two monomers (Fig EV5), oscillating around 1° (SD 9.5) in water, which is 17° smaller of the one measured for the crystallographic structure (pdb: 7jzj; Fig EV5). VP40 dimer flexibility is not constrained upon binding to the membrane; however, after binding to the bilayer, the angle distribution

was significantly ($P \leq 0.0001$) shifted to a value of 3.7° (SD 8.1) and 4.5° (SD 10.7) at pH 7.4 and 4.5, respectively.

Lipidomics of EBOV VLPs

Ebola virus VLPs composed of GP, VP40, and the nucleocapsid proteins NP, VP24, and VP35 were produced from HEK 293T cells and purified as described above. They were used at a final protein concentration of 880 ng/µl for lipidomics analysis. VLPs were subjected to lipid extractions using an acidic liquid–liquid extraction method (Blight & Dyer, [1959](#)) as described in Malek *et al* ([2021](#)). In order to ensure that similar amounts of lipids were extracted, a test extraction was performed to determine the concentration of PC as a bulk membrane lipid. Quantification was achieved by adding 1–3 internal lipid standards for each lipid class, with the standards resembling the structure of the endogenous lipid species. Of note, sample volumes were adjusted to ensure that all lipid standard to lipid species ratios were in a linear range of quantification. Typically, the standard to species ratios were within a range of > 0.1 to < 10. Following this approach, a relative quantification of lipid species was performed. Lipid standards were added prior to extractions, using a master mix consisting of 50 pmol phosphatidylcholine (PC, 13:0/13:0, 14:0/14:0, 20:0/20:0; 21:0/21:0, Avanti Polar Lipids), 50 pmol sphingomyelin (SM), d18:1 with N-acylated 13:0, 17:0, 25:0, semi-synthesized (Özbalci *et al*, [2013](#)), 100 pmol deuterated cholesterol (D7-cholesterol, Cambridge Isotope Laboratory), 30 pmol phosphatidylinositol (PI, 17:0/ 20:4, Avanti Polar Lipids), 25 pmol phosphatidylethanolamine (PE) and 25 pmol phosphatidylserine (PS); both 14:1/14:1, 20:1/20:1, 22:1/22:1, semi-synthesized (Özbalci *et al*, [2013](#)), 25 pmol diacylglycerol (DAG, 17:0/17:0, Larodan), 25 pmol cholesteryl ester (CE, 9:0, 19:0, 24:1, Sigma), and 24 pmol triacylglycerol (TAG, LM-6000/D5-17:0,17:1,17:1, Avanti Polar Lipids), 5 pmol ceramide (Cer, d18:1 with N-acylated 14:0, 17:0, 25:0, semi-synthesized (Özbalci *et al*, [2013](#)) or Cer d18:1/18:0-D3, Matreya) and 5 pmol glucosylceramide (HexCer; d18:1 with N-acylated 14:0, 19:0, 27:0, semi-synthesized or GlcCer d18:1/17:0, Avanti Polar Lipids), 5 pmol lactosylceramide (Hex2Cer, d18:1 with N-acylated C17 fatty acid), 10 pmol phosphatidic acid (PA, 17:0/20:4, Avanti Polar Lipids), 10 pmol phosphatidylglycerol (PG, 14:1/14:1, 20:1/20:1, 22:1/22:1), semi-synthesized (Özbalci *et al*, [2013](#)), and 5 pmol lysophosphatidylcholine (LPC, 17:1, Avanti Polar Lipids). The final CHCl$_3$ phase was evaporated under a gentle stream of nitrogen at 37°C. Samples were either directly subjected to mass spectrometric analysis or were stored at −20°C prior to analysis, which was typically done within 1–2 days after extraction. Lipid extracts were resuspended in 10 mM ammonium acetate in 60 µl methanol. Two µl aliquots of the resuspended lipids were diluted 1:10 in 10 mM ammonium acetate in methanol in 96-well plates (Eppendorf twin tec 96) prior to measurement. For cholesterol determinations, the remaining lipid extract was again evaporated and subjected to acetylation as previously described (Liebisch *et al*, [2006](#)). Samples were analyzed on an QTRAP 6500+ mass spectrometer (Sciex) with chip-based (HD-D ESI Chip, Advion Biosciences) electrospray infusion and ionization via a Triversa Nanomate (Advion Biosciences). MS settings and scan procedures are listed in Table EV2. Data evaluation was done using LipidView (Sciex) and an in-house-developed software (ShinyLipids).

Sequence alignment

To evaluate the conservation of the basic amino acid patch decorating the VP40 CTDs, we used Clustal Omega from EMBL-EBI (Sievers *et al*, [2011](#)) and applied a color code to display hydrophobicity (Kyte & Doolittle, [1982](#)).

Calibration of pHluorin fluorescence

HEK 293T cells were reverse transfected and seeded at a seeding density of 0.02×10^6 cells per well in a 96-well plate. Briefly, transfection mixtures were prepared containing a pCAGGS plasmid encoding pHluorin-VP40. After 15 min incubation at RT, HEK 293T cells were trypsinized and mixed with the transfection complexes before seeding on a fibronectin-coated 96 well plate. HNE buffers (10 mM HEPES, 100 mM NaCl, 1 mM EDTA) were prepared and calibrated to a pH of 3, 3.5, 4, 4.5, 5, 5.5, 6, 6.5, 7, 7.34, 7.52, and 8. Approximately 20 h post seeding, media was removed, the cells were washed once with HNE buffer at pH 7.34, and incubated for 45 min at 37°C, 5% CO$_2$, in the different HNE buffers. Fluorescence intensities were measured at 488 nm excitation using a Tecan plate reader. To calibrate the fluorescence of pHluorin at different pH, fluorescence was plotted against the pH.

Permeability of the HEK 293T cell plasma membrane

HEK 293T cells were reverse transfected as described above using pCAGGS plasmids encoding pHluorin-VP40 and influenza virus M2 (A/Udorn/307/1972 (subtype H3N2)) at a molar ratio of 1:0, 1:0.0002, 1:0.002, and 1:0.2. Approximately 20 h post seeding, the media was removed, and cells were washed once with HNE buffer, pH 7.34. The buffer was then exchanged with HNE buffer calibrated to pH 4.5, and fluorescence was immediately measured in 15 s intervals using a Tecan plate-reader.

Time-lapse microscopy of EBOV VLPs

Time-lapse microscopy was performed using a Leica SP8 confocal microscope with a 63× oil immersion objective. Purified pHluorin-labeled VLPs were added to a glow-discharged µ-Slide 8 well dish (ibidi) at a protein concentration of 10 ng/µl and were allowed to settle for 20 min at RT. They were then imaged using a 488 nm excitation laser and emission at 500–600 nm. Z-stacks were acquired in 15 s intervals for 30 min. To assess acidification kinetics, citric acid was added at a final concentration of 2.6 mM 2 min after starting the data acquisition. To assess acidification kinetics in the absence of the viral membrane, VLPs were incubated for 5 min with TX-100 at a final concentration of 0.1% before imaging.

Membrane permeability theory

We estimate the membrane permeability based on the geometry and pH equilibrium time of the VLPs. The membrane total proton flux, I, is proportional to the area of the VLPs, A_{VLP}, ion concentration difference between the buffer, C_B, and VLPs, C_{VLP}, $\Delta C(t) = C_B - C_{VLP}(t)$, and membrane permeability coefficient P_m (Deamer & Bramhall, [1986](#)),

$$I = P_m \bullet A_{VLP} \bullet \Delta C(t) \qquad (1)$$

It is easy to show that the protons concentration difference decays exponentially with time t,

$$\Delta C(t) = \Delta C_0 \bullet e^{-\frac{t}{\tau}} \qquad (2)$$

with the decay time constant $\tau = \frac{V_{VLP}}{P_m \bullet A_{VLP}}$, V_{VLP} the volume of the VLPs and ΔC_0 the initial concentration difference. The pH level is the logarithm of the protons concentration and can be related to the concentration difference as follows:

$$pH_{VLP}(t) = pH_{Buffer} - \log_{10}\left[1 - \frac{\Delta C_0}{C_B} \bullet e^{-\frac{t}{\tau}}\right] \qquad (3)$$

Next, we use a least-squares minimization procedure to fit the measured pH to Equation 3. We find the three minimization parameters pH_{Buffer}, $\frac{\Delta C_0}{C_B}$, and τ. Since the VLPs are either spherical or filamentous, we can derive the membrane permeability coefficient $P_m = \frac{R}{n \bullet \tau}$, with R the respective radius and n is either 2 for filamtoues VLPs or 3 for spherical VLPs and cells. The fitted decay times τ are presented in Appendix Fig S4B, and the VLPs radii are found using cryo-ET. In line with previous measurements of EBOV VLPs and virions (Wan *et al*, 2020), the filamentous VLPs had an average radius of 34 ± 4.5 nm ($n = 90$), while spherical particles are more heterogeneous in size, with a radius of 426 ± 100 nm ($n = 12$). A similar analysis was also performed on HEK 293T cells. The cells had a round shape. The radius was estimated using fluorescence microscopy to be 17.5 ± 2.5 nm.

Membrane fusion in the presence of a matrix layer

The fusion process involves three players—the membrane, the matrix layer, and the fusion proteins. In the following section, we describe the physical properties of these three, their interaction, and the fusion pathway in the presence of a matrix layer. We determine the effect of the matrix layer on fusion rate by calculating the magnitude of the two major energy barriers to membrane fusion (Jahn & Grubmüller, 2002; Chernomordik & Kozlov, 2008; Fuhrmans *et al*, 2015) stalk formation and fusion pore expansion in the presence of the matrix layer and compare it to the matrix-free state.

Description of the fusion site and the fusion process

The fusion reaction starts when the fusion proteins bring the EBOV and endosomal membranes to proximity and drive the merger of only the proximal monolayers. As a result, the membrane and matrix layer deform and locally detach. The fusion site is axially symmetric; its cross-section is illustrated in Fig 4B. The two fusing membranes form a junction in the center of the stalk, with the two membrane mid-planes forming a corner with a 45° angle. As a result, the lipid tails are sheared and splayed to prevent voids in the hydrocarbon tail moiety (Kozlovsky & Kozlov, 2002). The shear and splay magnitude decays within several nanometers from the stalk and smoothly connects to the flat surrounding membranes. After the stalk has formed, it radially expands to an equilibrium radius R_D by bringing the two inner monolayers into contact along a joint mid-plane, a state called hemifusion diaphragm (Kozlovsky

et al, 2002; Golani *et al*, 2021). The rim of the diaphragm is the three-way junction between the diaphragm and the two fusing membranes. The lipid monolayer deformations are continuous; therefore, we explicitly require that the magnitude of lipid splay, saddle-splay, and shear are continuous everywhere in our numerical calculations. The matrix layer adheres to the membrane by electrostatic interaction, and it can locally detach from it at the vicinity of the stalk and the diaphragm rim junction to avoid substantial deformation there. Thus, the matrix is not necessarily parallel to the membrane and can bend independently. The deformation of both the membranes and the matrix layer vanishes at the edge of the fusion site and connects smoothly to a flat surrounding membrane and matrix layer. The membrane fluidity in the lateral direction allows the matrix layer to slide on it freely as the fusion process progresses. The fusion reaction ends by opening and expending a membrane pore within the diaphragm, which must involve the detachment of the favorable bounds between the EBOV luminal monolayer and the VP40 matrix layer.

The lipid membrane

We model the lipid membrane using the well-established theory of lipid tilt, splay, and saddle-splay (Helfrich, 1973; Hamm & Kozlov, 2000). The membrane is composed of two monolayers that share a joint mid-plane. The orientation of the lipids in the two monolayers is independent and is given by the lipid director vector, $\hat{n}$. The lipid tilt vector, $\vec{t} = \frac{\hat{n}}{\hat{n} \bullet \hat{N}} - \hat{N}$, characterizes the shear magnitude and its direction (Hamm & Kozlov, 1998), with $\hat{N}$ the midplane normal. The monolayer dividing plane is parallel to the membrane midplane and is located at a distance of $\delta = \delta_0\sqrt{1 + \vec{t}^2}$ from it, with δ_0 the length of the undeformed monolayer tails. The lipid splay and saddle splay are derived from the splay tensor, $\tilde{b}_\alpha^\beta = \nabla_\alpha n^\beta$, where the sub- and superscripts denote, respectively, the co- and contra-variant components in the local coordinate basis of the monolayer dividing plane (Hamm & Kozlov, 2000). Lipid splay is the trace of the splay tensor $\tilde{J} = \tilde{b}_\alpha^\alpha$, and lipid saddle-splay is its determinant it $\tilde{K} = \det \tilde{b}_\alpha^\beta$. The energy density with respect to the flat tilt-free configuration associated with these deformations is given by Hamm & Kozlov (2000) and Terzi *et al* (2019),

$$f_m = \frac{1}{2}\kappa\left(J\,2 - 2\,J\,J_{sm}\right) + \bar{\kappa}\tilde{K} + \frac{1}{2}\kappa_t\,\vec{t}^2. \qquad (4)$$

The bending rigidity of the monolayer, κ_m, has a typical value of $10\,k_BT$ (Dimova, 2014), saddle-splay modulus, $\bar{\kappa}_m$, and tilt modulus, κ_t, cannot be directly measured and are indirectly estimated. The ratio between saddle-splay modulus and bending rigidity is between -1 and 0 (Templer *et al*, 1998; Terzi *et al*, 2019). The ratio between the bending rigidity to tilt modulus gives a typical tilt decay length of $l = \sqrt{\kappa/\kappa_t}$, typically between 1 and 2 nm (Terzi & Deserno, 2017). Here we use $l = 1.5$ nm and $\bar{\kappa}/\kappa = -0.5$. The monolayer spontaneous curvature, J_{sm}, is the averaged intrinsic curvature of its constituting lipids,

$$\sum_{i=1}^{i=M} \zeta_i \varphi_i. \qquad (5)$$

M is the total number of lipid components, and ζ_i and φ_i are the intrinsic curvature and mole fraction of the i lipid components, respectively. The lipid composition is found using lipidomic data of

the endosomal and viral membranes (Fig 1J). The intrinsic curvature of the most abundant lipids is $\zeta_{PC} \approx -0.1$ nm^{-1} for phosphatidylcholine (PC; Chen & Rand, 1997; Szule et al, 2002), cholesterol $\zeta_{CHOL} \approx -0.5$ nm^{-1} (Chen & Rand, 1997; Kollmitzer et al, 2013), phosphatidylethanolamine (PE) with $\zeta_{PE} \approx -0.35$ nm^{-1} (Leikin et al, 1996; Kollmitzer et al, 2013), and sphingomyelin $\zeta_{SM} \approx -0.1$ nm^{-1} (Leikin et al, 1996). We find that the endosomal and Ebola virus both have monolayer spontaneous curvature of roughly $J_{sm} = -0.22$ nm^{-1}.

The overall membrane deformation energy is given by the integration of Equation 4 over the area of both monolayers independently,

$$F_{Mem} = \int f_+ dA_+ + \int f_+ dA_+ \tag{6}$$

The first and second integral in Equation 6 is performed over the upper and lower monolayer area, respectively.

The matrix layer

We model the matrix layer as a thin, uniform rigid elastic shell with a flat resting configuration. The matrix can avoid the sharp corners in the vicinity of the stalk and diaphragm rim by local detachment from the membrane. These allow the matrix to avoid strong shear deformations. The elastic energy of matrix deformation up to quadratic order in the area strain, ϵ, and in principle curvatures, c_1 and c_2, is given by Landau & Lifshitz (1970),

$$F_{mat} = \frac{Yd}{2(1-\nu)} \int \frac{1}{2} \epsilon^2 dA_0 \\ + \frac{Yd^3}{12(1-\nu^2)} \int \left[\frac{1}{2}(c_1+c_2)^2 - (1-\nu)c_1 \cdot c_2 \right] dA \tag{7}$$

with dA_0 and dA are the area elements of the undeformed and deformed states, d is the matrix thickness, Y is the Young's modulus, and ν is the Poisson's ratio. We consider only stretching and bending deformations and explicitly prohibit shear. The thickness of the VP40 matrix layer is estimated to be $d = 4$ nm based on the cryo-ET data presented here (Fig 1A–H). The Young's modulus and Poisson ratio of the VP40 matrix layer was never measured, but we estimate them to be within the same magnitude as other viruses with similar matrix layer structures, such as M1 of influenza virus. The VP40 matrix layer Poisson's ratio is taken as $\nu = 0.5$, and the Youngs modulus is in the range 5–22 MPa (Li et al, 2011; Schaap et al, 2012). With that, we estimate the stretching modulus of the VP40 matrix layer in the range of $\frac{Yd}{2(1-\nu)} \sim 20 \rightarrow 80$ mN/m, and the pure bending contribution with modulus in the range of $\frac{Yd^3}{24(1-\nu^2)} \sim 8 \rightarrow 35$ k$_B$T.

The matrix layer and the membrane can locally detach in the vicinity of the stalk and diaphragm rim to avoid substantial deformation there. Besides these regions, the matrix interacts continuously with the membrane since the VP40 matrix layer is tightly packed. Inspired by the MD simulations (Fig 2E), we describe the VP40-membrane interaction energy density with Lennard–Jones-like potential,

$$U_{int} = \int u_0 \left[\left(\frac{z_0}{z} \right)^{12} - 2 \left(\frac{z_0}{z} \right)^6 \right] dA \tag{8}$$

with the integral performed on the area of the matrix layer, dA. z is the distance from the monolayer dividing plane to the mid-plane of the VP40 layer, and $z_0 = 4$ nm is the resting length obtained from

sub-tomogram averaging and the MD simulations (Fig 4H). The interaction energy density, u_0, is estimated from the MD simulations as the free energy of a single VP40 dimer at $z = z_0$ (11 k$_B$T for pH 7.4 and 6.5 k$_B$T for pH 4.5, Fig 2E) divided by the density of VP40 dimers obtained from the cryo-ET data (Fig 1I), we find $u_0 = 0.2$ k$_b$T•nm^{-2} at pH 7.4 and $u_0 = 0.1$ k$_b$T•nm^{-2} at pH 4.5.

Computational procedure

Our computational approach is based on previous works (Golani et al, 2021; Zucker et al, 2021) and published as open-source code on GitHub (https://github.com/GonenGolani/Fusion_Solver), where further details can be found. The calculation involves three parts. We start by simulating the stalk shape and find its minimal energy configuration. Next, we allow the stalk to expand to hemifusion diaphragm, and finally, we calculate the energy barrier of pore formation based on the membrane stress and the interaction energy with the VP40 matrix layer in the diaphragm.

The stalk energy barrier represents the minimal mechanical work needed to merge the proximal monolayers. We calculate the hemifusion stalk shape and its formation energy by setting the membrane in stalk configuration. Then, we minimize the sum of the membrane and matrix interaction deformation energies (Equations 7 and (8)) while requiring that $R_D = 0$,

$$E_{stalk}^* = \min[F_{Mem} + F_{mat} + U_{int}] \tag{9}$$

after the stalk has formed, we release the constrain on R_D and allow the system to spontaneously relaxes to a hemifusion diaphragm. The matrix layer can remain attached to the diaphragm or detached.

We calculate the fusion-pore formation energy barrier based on the stress in the hemifusion diaphragm. To facilitate our computation, we assume that the pore formation is initiated at the center of the diaphragm and that the fast fluctuation in pore size does not change the hemifusion diaphragm and matrix layer equilibrium shapes. The pore must expand to the majority of the diaphragm before it overcomes the critical energy, so the initiation point is mainly irrelevant to the magnitude energy barrier. However, since the pores are more likely to form in the vicinity of the diaphragm rim, where stress is maximal, our estimation should be considered a slight overestimation of the actual energy barrier. With this assumption, the energy of pore opening to radius ρ is thus given by

$$E_{pore}(\rho) = 2\pi\rho\lambda - \pi \int_{\rho'=0}^{\rho'=\rho} \gamma(\rho')\rho' d\rho', \tag{10}$$

with λ, the pore rim line-tension magnitude, being independent of the matrix layer or the membrane shape. In our simulations, we take it to be $\lambda = 12$ pN (Portet & Dimova, 2010). The second term in Equation 10 is the energy gained by removing lipids from the stressed diaphragm and relocating them to the surrounding membranes. The stress contains two contributions: the relaxation of the splay, saddle-splay, and shear of the lipids compared to the surrounding membranes and the detachment from the matrix layer,

$$\gamma(\rho) = f_+(\rho) + f_-(\rho) + u(\rho). \tag{11}$$

with f_+ and f_- the energy deformation density of the upper and lower monolayer (Equation 4), respectively, and u the interaction

energy density with the matrix (Equation 8). The pore formation energy barrier is the maxima of $E_{pore}(\rho)$,

$$E^*_{pore}(\rho = \rho^*) = \max[E_{pore}]. \tag{12}$$

We find the stress (Equation 11) based on the equilibrium shape of the diaphragm, and Equation 12 is found by numerically integrating Equation 10 and finding the maximum.

Beta-lactamase assay

Huh7 cells were seeded on a 96-well plate coated with $2\,\mu g$ fibronectin in $1\times PBS$ at a density of 0.02×10^6 cells per well. 24 h post seeding, the media of inhibitor-treated cells were replaced with 25 mM $NHCl_4$ in DMEM media (ThermoFisher Scientific) supplemented with 10% (v/v) FBS and 100 U/ml penicillin–streptomycin (ThermoFisher Scientific), and cells were incubated for 1.5 h at 37°C, 5% CO_2.

Same amounts of purified beta-lactamase (BlaM)-containing VLPs were either untreated, treated with low pH, thermolysin, or a combination of low pH and thermolysin. For the thermolysin-treatment, $500\,\mu g/ml$ thermolysin (ThermoFisher Scientific), reconstituted in H_2O and filtered through a $0.22\,\mu m$ membrane filter, was added to the VLPs for 30 min at 37°C. To quench the reaction, $300\,\mu g/ml$ phosphoramidon was added for 10 min at 37°C. For the low pH treatment, citric acid prepared in HNE buffer (10 mM HEPES, 100 mM NaCl, 1 mM EDTA) was added in a final concentration of 1.67 mM to the VLPs for 30 min at 37°C. The BlaM-VLPs were immediately placed on ice until infection.

For infection, the media of all cells were removed, and $50\,\mu l$ pretreated BlaM-VLP solution was added to each well and the plate was centrifuged for 30 min at $200\,g$, 20°C (Beckmann). BlaM-VLP solutions were immediately removed and replaced with $100\,\mu l$ media with and without 25 mM NH_4Cl. Cells were incubated for 1.5 h at 37°C, 5% CO_2, before freshly preparing the BlaM dye from the LiveBLAzer™ FRET-B/G Loading Kit with CCF4-AM (ThermoFisher Scientific) supplemented with probenecid (Invitrogen) according to the protocol provided by the manufacturer. $20\,\mu l$ of the BlaM mix was added per well. After incubation at 11°C for 12–14 h, the cells were briefly checked for viability using a Nikon microscope and detached for 5–10 min using trypsin–EDTA at 37°C. Cells were harvested and washed with $3\times$ with PBS before performing FACS using a BD FACS Celesta Cell Analyzer (BD Biosciences).

Data availability

Electron tomography data were deposited to EMDB (EMD-15268, http://www.ebi.ac.uk/pdbe/entry/EMD-15268; EMD-15244, http://www.ebi.ac.uk/pdbe/entry/EMD-15244). Additional data and material related to this publication may be obtained upon request. Atomistic molecular dynamics simulations of initial structures and topology files were deposited to Zenodo (https://doi.org/10.5281/zenodo.7652685).

Expanded View for this article is available online.

Author contributions

Sophie L Winter: Conceptualization; formal analysis; validation; investigation; visualization; methodology; writing – original draft; writing – review and editing. **Gonen Golani:** Conceptualization; software; validation; investigation; visualization; methodology; writing – original draft; writing – review and editing. **Fabio Lolicato:** Conceptualization; software; formal analysis; investigation; visualization; methodology; writing – review and editing. **Melina Vallbracht:** Investigation; methodology; writing – review and editing. **Keerthihan Thiyagarajah:** Formal analysis; methodology. **Samy Sid Ahmed:** Formal analysis; investigation; methodology. **Christian Lüchtenborg:** Methodology. **Oliver T Fackler:** Supervision; funding acquisition; writing – review and editing. **Britta Brügger:** Supervision; funding acquisition. **Thomas Hoenen:** Formal analysis; investigation; methodology; writing – review and editing. **Walter Nickel:** Supervision; funding acquisition; writing – review and editing. **Ulrich S Schwarz:** Supervision; funding acquisition; writing – review and editing. **Petr Chlanda:** Conceptualization; formal analysis; supervision; funding acquisition; validation; investigation; writing – original draft; project administration; writing – review and editing.

Disclosure and competing interests statement

The authors declare that they have no conflict of interest.

References

Abraham MJ, Murtola T, Schulz R, Páll S, Smith JC, Hess B, Lindah E (2015) Gromacs: high performance molecular simulations through multi-level parallelism from laptops to supercomputers. *SoftwareX* 1–2: 19–25

Adu-Gyamfi E, Soni SP, Xue Y, Digman MA, Gratton E, Stahelin RV (2013) The ebola virus matrix protein penetrates into the plasma membrane: a key step in viral protein 40 (VP40) oligomerization and viral egress. *J Biol Chem* 288: 5779–5789

Amiar S, Husby ML, Wijesinghe KJ, Angel S, Bhattarai N, Gerstman BS, Chapagain PP, Li S, Stahelin RV (2021) Lipid-specific oligomerization of the Marburg virus matrix protein VP40 is regulated by two distinct interfaces for virion assembly. *J Biol Chem* 296: 100796

Banerjee I, Miyake Y, Philip Nobs S, Schneider C, Horvath P, Kopf M, Matthias P, Helenius A, Yamauchi Y (2014) Influenza a virus uses the aggresome processing machinery for host cell entry. *Science* 346: 473–477

Bharat TAM, Noda T, Riches JD, Kraehling V, Kolesnikova L, Becker S, Kawaoka Y, Briggs JAG (2012) Structural dissection of Ebola virus and its assembly

determinants using cryo-electron tomography. *Proc Natl Acad Sci U S A* 109: 4275–4280

Blight EG, Dyer WJ (1959) A rapid method of total lipid extraction and purification. *Can J Biochem Physiol* 37: 911–917

Bonomi M, Bussi G, Camilloni C, Tribello GA, Banáš P, Barducci A, Bernetti M, Bolhuis PG, Bottaro S, Branduardi D *et al* (2019) (2019) promoting transparency and reproducibility in enhanced molecular simulations. *Nat Methods* 168: 670–673

Booth TF, Rabb MJ, Beniac DR (2013) How do filovirus filaments bend without breaking? *Trends Microbiol* 21: 583–593

Bornholdt ZA, Noda T, Abelson DM, Halfmann P, Wood MR, Kawaoka Y, Saphire EO (2013) Structural rearrangement of ebola virus vp40 begets multiple functions in the virus life cycle. *Cell* 154: 763–774

Brecher M, Schornberg KL, Delos SE, Fusco ML, Saphire EO, White JM (2012) Cathepsin cleavage potentiates the Ebola virus glycoprotein to undergo a subsequent fusion-relevant conformational change. *J Virol* 86: 364–372

Carette JE, Raaben M, Wong AC, Herbert AS, Obernosterer G, Mulherkar N, Kuehne AI, Kranzusch PJ, Griffin AM, Ruthel G *et al* (2011) Ebola virus entry requires the cholesterol transporter Niemann-pick C1. *Nature* 477: 340–343

Castaño-Díez D (2017) The Dynamo package for tomography and subtomogram averaging: components for MATLAB, GPU computing and EC2 Amazon web Services. *Acta Crystallogr D Struct Biol* 73: 478–487

Castaño-Díez D, Kudryashev M, Arheit M, Stahlberg H (2012) Dynamo: a flexible, user-friendly development tool for subtomogram averaging of cryo-EM data in high-performance computing environments. *J Struct Biol* 178: 139–151

Chen Z, Rand RP (1997) The influence of cholesterol on phospholipid membrane curvature and bending elasticity. *Biophys J* 73: 267–276

Chernomordik LV, Kozlov MM (2008) Mechanics of membrane fusion. *Nat Struct Mol Biol* 15: 675–683

Chernomordik LV, Zimmerberg J, Kozlov MM (2006) Membranes of the world unite! *J Cell Biol* 175: 201–207

Côté M, Misasi J, Ren T, Bruchez A, Lee K, Filone CM, Hensley L, Li Q, Ory D, Chandran K *et al* (2011) Small molecule inhibitors reveal Niemann-pick C1 is essential for Ebola virus infection. *Nature* 477: 344–348

Coutsias EA, Seok C, Jacobson MP, Dill KA (2004) A kinematic view of loop closure. *J Comput Chem* 25: 510–528

Deamer DW (1987) Proton permeation of lipid bilayers. *J Bioenerg Biomembr* 19: 457–479

Deamer DW, Bramhall J (1986) Permeability of lipid bilayers to water and ionic solutes. *Chem Phys Lipids* 40: 167–188

DeCoursey TE (2008) Voltage-gated proton channels. *Cell Mol Life Sci* 65: 2554–2573

Del Vecchio K, Frick CT, Jeevan Gc XB, Oda S, Bernard Gerstman XS, Erica Ollmann Saphire X, Prem Chapagain XP, Robert Stahelin XV (2018) A cationic, C-terminal patch and structural rearrangements in Ebola virus matrix VP40 protein control its interactions with phosphatidylserine. *J Biol Chem* 293: 3335–3349

Dimova R (2014) Recent developments in the field of bending rigidity measurements on membranes. *Adv Colloid Interface Sci* 208: 225–234

Dube D, Brecher MB, Delos SE, Rose SC, Park EW, Schornberg KL, Kuhn JH, White JM (2009) The primed ebolavirus glycoprotein (19-Kilodalton GP 1,2): sequence and residues critical for host cell binding. *J Virol* 83: 2883–2891

Essmann U, Perera L, Berkowitz ML, Darden T, Lee H, Pedersen LG (1995) A smooth particle mesh Ewald method. *J Chem Phys* 103: 8577–8593

Fäßler F, Zens B, Hauschild R, Schur FKM (2020) 3D printed cell culture grid holders for improved cellular specimen preparation in cryo-electron microscopy. *J Struct Biol* 212: 107633 https://doi.org/10.1016/j.jsb.2020.107633

Feldmann H, Klenk HD (1996) Marburg and Ebola viruses. *Adv Virus Res* 47: 1–52

Fontana J, Steven AC (2013) At low pH, influenza virus matrix protein M1 undergoes a conformational change prior to dissociating from the membrane. *J Virol* 87: 5621–5628

Fuhrmans M, Marelli G, Smirnova YG, Müller M (2015) Mechanics of membrane fusion/pore formation. *Chem Phys Lipids* 185: 109–128

Geisbert TW, Jahrling PB (1995) Differentiation of filoviruses by electron microscopy. *Virus Res* 39: 129–150

Golani G, Leikina E, Melikov K, Whitlock JM, Gamage DG, Luoma-Overstreet G, Millay DP, Kozlov MM, Chernomordik LV (2021) Myomerger promotes fusion pore by elastic coupling between proximal membrane leaflets and hemifusion diaphragm. *Nat Commun* 12: 1–18

Greber UF, Singh I, Helenius A (1994) Mechanisms of virus uncoating. *Trends Microbiol* 2: 52–56

Hagen WJH, Wan W, Briggs JAG (2017) Implementation of a cryo-electron tomography tilt-scheme optimized for high resolution subtomogram averaging. *J Struct Biol* 197: 191–198

Hamm M, Kozlov MM (1998) Tilt model of inverted amphiphilic mesophases. *Eur Phys J B* 6: 519–528

Hamm M, Kozlov MM (2000) Elastic energy of tilt and bending of fluid membranes. *Eur Phys J E* 3: 323–335

Harrison SC (2008) Viral membrane fusion. *Nat Struct Mol Biol* 15: 690–698

Helfrich W (1973) Elastic properties of lipid bilayers: theory and possible experiments. *Z Naturforsch C* 28: 693–703

Hess B, Bekker H, Berendsen HJC, Fraaije JGEM (1997) LINCS: a linear constraint solver for molecular simulations. *J Comput Chem* 18: 1463–1472

Hoover WG (1985) Canonical dynamics: equilibrium phase-space distributions. *Phys Rev A* 31: 1695–1697

Huang J, Mackerell AD (2013) CHARMM36 all-atom additive protein force field: validation based on comparison to NMR data. *J Comput Chem* 34: 2135–2145

Huang J, Rauscher S, Nawrocki G, Ran T, Feig M, De Groot BL, Grubmüller H, MacKerell AD (2016) CHARMM36m: an improved force field for folded and intrinsically disordered proteins. *Nat Methods* 14: 71–73

Hub JS, De Groot BL, Van Der Spoel D (2010) G-whams-a free weighted histogram analysis implementation including robust error and autocorrelation estimates. *J Chem Theory Comput* 6: 3713–3720

Humphrey W, Dalke A, Schulten K (1996) VMD: visual molecular dynamics. *J Mol Graph* 14: 33–38

Jahn R, Grubmüller H (2002) Membrane fusion. *Curr Opin Cell Biol* 14: 488–495

Jeevan BG, Gerstman BS, Stahelin RV, Chapagain PP (2016) The Ebola virus protein VP40 hexamer enhances the clustering of PI(4,5)P2 lipids in the plasma membrane. *Phys Chem Chem Phys* 18: 28409–28417

Jeevan BG, Gerstman BS, Chapagain PP (2017) Membrane association and localization dynamics of the Ebola virus matrix protein VP40. *Biochim Biophys Acta Biomembr* 1859: 2012–2020

Jo S, Kim T, Iyer VG, Im W (2008) CHARMM-GUI: a web-based graphical user interface for CHARMM. *J Comput Chem* 29: 1859–1865

Jo S, Lim JB, Klauda JB, Im W (2009) CHARMM-GUI membrane builder for mixed bilayers and its application to yeast membranes. *Biophys J* 97: 50–58

Johnson KA, Taghon GJF, Scott JL, Stahelin RV (2016) The Ebola virus matrix protein, VP40, requires phosphatidylinositol 4,5-bisphosphate (PI(4,5)P 2)

for extensive oligomerization at the plasma membrane and viral egress. *Sci Rep* 6: 1–14

Jones DM, Padilla-Parra S (2016) The β-lactamase assay: harnessing a FRET biosensor to analyse viral fusion mechanisms. *Sensors* 16: 950

Jorgensen WL, Chandrasekhar J, Madura JD, Impey RW, Klein ML (1983) Comparison of simple potential functions for simulating liquid water. *J Chem Phys* 79: 926–935

Klein S, Cortese M, Winter S, Wachsmuth-Melm M, Neufeldt C, Cerikan B, Stanifer M, Boulant S, Bartenschlager R, Chlanda P (2020a) SARS-CoV-2 structure and replication characterized by in situ cryo-electron tomography. *Nat Commun* 11: 5885

Klein S, Wimmer B, Winter SL, Kolovou A, Laketa V, Chlanda P (2020b) Post-correlation on-lamella cryo-CLEM reveals the membrane architecture of lamellar bodies. *Commun Biol* 4: 137

Kollmitzer B, Heftberger P, Rappolt M, Pabst G (2013) Monolayer spontaneous curvature of raft-forming membrane lipids. *Soft Matter* 9: 10877–10884

Kozlovsky Y, Kozlov MM (2002) Stalk model of membrane fusion: solution of energy crisis. *Biophys J* 82: 882–895

Kozlovsky Y, Chernomordik LV, Kozlov MM (2002) Lipid intermediates in membrane fusion: formation, structure, and decay of hemifusion diaphragm. *Biophys J* 83: 2634–2651

Kyte J, Doolittle RF (1982) A simple method for displaying the hydropathic character of a protein. *J Mol Biol* 157: 105–132

Landau LD, Lifshitz EM (1970) *Theory of elasticity*. New York, NY: Pergamon Press

Lee JE, Saphire EO (2009) Ebolavirus glycoprotein structure and mechanism of entry. *Future Virol* 4: 621–635

Lee J, Kreutzberger AJB, Odongo L, Nelson EA, Nyenhuis DA, Kiessling V, Liang B, Cafiso DS, White JM, Tamm LK (2021) Ebola virus glycoprotein interacts with cholesterol to enhance membrane fusion and cell entry. *Nat Struct Mol Biol* 28: 181–189

Leikin S, Kozlov MM, Fuller NL, Rand RP (1996) Measured effects of diacylglycerol on structural and elastic properties of phospholipid membranes. *Biophys J* 71: 2623–2632

Li S, Eghiaian F, Sieben C, Herrmann A, Schaap IAT (2011) Bending and puncturing the influenza lipid envelope. *Biophys J* 100: 637–645

Li S, Sieben C, Ludwig K, Höfer CT, Chiantia S, Herrmann A, Eghiaian F, Schaap IAT (2014) PH-ontrolled two-step uncoating of influenza virus. *Biophys J* 106: 1447–1456

Liebisch G, Binder M, Schifferer R, Langmann T, Schulz B, Schmitz G (2006) High throughput quantification of cholesterol and cholesteryl ester by electrospray ionization tandem mass spectrometry (ESI-MS/MS). *Biochim Biophys Acta* 1761: 121–128

Lozach PY, Huotari J, Helenius A (2011) Late-penetrating viruses. *Curr Opin Virol* 1: 35–43

Mahamid J, Tegunov D, Maiser A, Arnold J, Leonhardt H, Plitzko JM, Baumeister W (2019) Liquid-crystalline phase transitions in lipid droplets are related to cellular states and specific organelle association. *Proc Natl Acad Sci U S A* 116: 16866–16871

Malek M, Wawrzyniak AM, Koch P, Lüchtenborg C, Hessenberger M, Sachsenheimer T, Jang W, Brügger B, Haucke V (2021) Inositol triphosphate-triggered calcium release blocks lipid exchange at endoplasmic reticulum-Golgi contact sites. *Nat Commun* 12: 2673

Manzoor R, Igarashi M, Takada A (2017) Influenza a virus M2 protein: roles from ingress to egress. *Int J Mol Sci* 18: 2649

Mastronarde D (2005) Automated electron microscope tomography using robust prediction of specimen movements. *J Struct Biol* 152: 36–51

Mastronarde DN, Held SR (2017) Automated tilt series alignment and tomographic reconstruction in IMOD. *J Struct Biol* 197: 102–113

Miesenböck G, De Angelis DA, Rothman JE (1998) Visualizing secretion and synaptic transmission with pH-sensitive green fluorescent proteins. *Nature* 394: 192–195

Miller EH, Obernosterer G, Raaben M, Herbert AS, Deffieu MS, Krishnan A, Ndungo E, Sandesara RG, Carette JE, Kuehne AI *et al* (2012) Ebola virus entry requires the host-programmed recognition of an intracellular receptor. *EMBO J* 31: 1947–1960

Mingo RM, Simmons JA, Shoemaker CJ, Nelson EA, Schornberg KL, D'Souza RS, Casanova JE, White JM (2015a) Ebola virus and severe acute respiratory syndrome coronavirus display late cell entry kinetics: evidence that transport to NPC1$^+$ Endolysosomes is a rate-defining step. *J Virol* 89: 2931–2943

Mingo RM, Simmons JA, Shoemaker CJ, Nelson EA, Schornberg KL, D'Souza RS, Casanova JE, White JM (2015b) EBOV and SARS-CoV display late cell entry kinetics: evidence that transport to NPC1 + Endolysosomes is a rate-defining step. *J Virol* 89: 2931–2943

Nanbo A, Imai M, Watanabe S, Noda T, Takahashi K, Neumann G, Halfmann P, Kawaoka Y (2010) Ebolavirus is internalized into host cells via macropinocytosis in a viral glycoprotein-dependent manner. *PLoS Pathog* 6: e1001121

Nguyen TL, Schoehn G, Weissenhorn W, Hermone AR, Burnett JC, Panchal RG, McGrath C, Zaharevitz DW, Aman MJ, Gussio R *et al* (2005) An all-atom model of the pore-like structure of hexameric VP40 from Ebola: structural insights into the monomer-hexamer transition. *J Struct Biol* 151: 30–40

van Niel G, Bergam P, Di Cicco A, Hurbain I, Lo Cicero A, Dingli F, Palmulli R, Fort C, Potier MC, Schurgers LJ *et al* (2015) Apolipoprotein E regulates amyloid formation within endosomes of pigment cells. *Cell Rep* 13: 43–51

Noda T, Sagara H, Suzuki E, Takada A, Kida H, Kawaoka Y (2002) Ebola virus VP40 drives the formation of virus-like filamentous particles along with GP. *J Virol* 76: 4855–4865

Norris MJ, Husby ML, Kiosses WB, Yin J, Saxena R, Rennick LJ, Heiner A, Harkins SS, Pokhrel R, Schendel SL *et al* (2022) Measles and Nipah virus assembly: specific lipid binding drives matrix polymerization. *Sci Adv* 8: eabn1440

Özbalci C, Sachsenheimer T, Brügger B (2013) Quantitative analysis of cellular lipids by nano-electrospray ionization mass spectrometry. *Methods Mol Biol* 1033: 3–20

Panchal RG, Ruthel G, Kenny TA, Kallstrom GH, Lane D, Badie SS, Li L, Bavari S, Aman MJ (2003) In vivo oligomerization and raft localization of Ebola virus protein VP40 during vesicular budding. *Proc Natl Acad Sci U S A* 100: 15936–15941

Parrinello M, Rahman A (1981) Polymorphic transitions in single crystals: a new molecular dynamics method. *J Appl Phys* 52: 7182–7190

Pastor RW, MacKerell AD (2011) Development of the CHARMM force field for lipids. *J Phys Chem Lett* 2: 1526–1532

Pavadai E, Gerstman BS, Chapagain PP (2018) A cylindrical assembly model and dynamics of the Ebola virus VP40 structural matrix. *Sci Rep* 8: 9776

Portet T, Dimova R (2010) A new method for measuring edge tensions and stability of lipid bilayers: effect of membrane composition. *Biophys J* 99: 3264–3273

Ruigrok RWH, Schoehn G, Dessen A, Forest E, Volchkov V, Dolnik O, Klenk HD, Weissenhorn W (2000) Structural characterization and membrane binding properties of the matrix protein VP40 of Ebola virus. *J Mol Biol* 300: 103–112

Schaap IAT, Eghiaia F, Des George A, Veigel C (2012) Effect of envelope proteins on the mechanical properties of influenza virus. *J Biol Chem* 287: 41078–41088

Scianimanico S, Schoehn G, Timmins J, Ruigrok RHW, Klenk HD, Weissenhorn W (2000) Membrane association induces a conformational change in the Ebola virus matrix protein. *EMBO J* 19: 6732–6741

Sievers F, Wilm A, Dineen D, Gibson TJ, Karplus K, Li W, Lopez R, McWilliam H, Remmert M, Söding J *et al* (2011) Fast, scalable generation of high-quality protein multiple sequence alignments using Clustal omega. *Mol Syst Biol* 7: 539

Simmons JA, D'Souza RS, Ruas M, Galione A, Casanova JE, White JM (2015) Ebolavirus glycoprotein directs fusion through NPC1- Endolysosomes. *J Virol* 90: 605–610

Søndergaard CR, Olsson MHM, Rostkowski M, Jensen JH (2011) Improved treatment of ligands and coupling effects in empirical calculation and rationalization of p K a values. *J Chem Theory Comput* 7: 2284–2295

Soni SP, Stahelin RV (2014) The Ebola virus matrix protein VP40 selectively induces Vesiculation from phosphatidylserine-enriched membranes. *J Biol Chem* 289: 33590–33597

Stahelin RV (2014) Membrane binding and bending in Ebola VP40 assembly and egress. *Front Microbiol* 5: 300

Stauffer CE (1971) The effect of pH on thermolysin activity. *Arch Biochem Biophys* 147: 568–570

Szule JA, Fuller NL, Peter Rand R (2002) The effects of acyl chain length and saturation of diacylglycerols and phosphatidylcholines on membrane monolayer curvature. *Biophys J* 83: 977–984

Takamatsu Y, Kolesnikova L, Becker S (2018) Ebola virus proteins NP, VP35, and VP24 are essential and sufficient to mediate nucleocapsid transport. *Proc Natl Acad Sci U S A* 115: 1075–1080

Templer RH, Khoo BJ, Seddon JM (1998) Gaussian curvature modulus of an amphiphilic monolayer. *Langmuir* 14: 7427–7434

Terzi MM, Deserno M (2017) Novel tilt-curvature coupling in lipid membranes. *J Chem Phys* 147: 084702

Terzi MM, Ergüder MF, Deserno M (2019) A consistent quadratic curvature-tilt theory for fluid lipid membranes. *J Chem Phys* 151: 164108

Torrie GM, Valleau JP (1974) Monte Carlo free energy estimates using non-Boltzmann sampling: application to the sub-critical Lennard-Jones fluid. *Chem Phys Lett* 28: 578–581

Torrie GM, Valleau JP (1977) Nonphysical sampling distributions in Monte Carlo free-energy estimation: umbrella sampling. *J Comput Phys* 23: 187–199

Tribello GA, Bonomi M, Branduardi D, Camilloni C, Bussi G (2014) PLUMED 2: new feathers for an old bird. *Comput Phys Commun* 185: 604–613

Tsui FC, Ojcius DM, Hubbell WL (1986) The intrinsic pKa values for phosphatidylserine and phosphatidylethanolamine in phosphatidylcholine host bilayers. *Biophys J* 49: 459–468

Wan W, Kolesnikova L, Clarke M, Koehler A, Noda T, Becker S, Briggs JAG (2017) Structure and assembly of the Ebola virus nucleocapsid. *Nature* 551: 394–397

Wan W, Clarke M, Norris MJ, Kolesnikova L, Koehler A, Bornholdt ZA, Becker S, Saphire EO, Briggs JAG (2020) Ebola and Marburg virus matrix layers are locally ordered assemblies of VP40 dimers. *Elife* 9: e59225

Welsch S, Kolesnikova L, Krähling V, Riches JD, Becker S (2010) Electron tomography reveals the steps in filovirus budding. *PLoS Pathog* 6: 1000875

Winter SL, Chlanda P (2021) Dual-axis Volta phase plate cryo-electron tomography of Ebola virus-like particles reveals Actin-VP40 interactions. *J Struct Biol* 213: 107742

Yamauchi Y, Greber UF (2016) Principles of virus Uncoating: cues and the snooker ball. *Traffic* 17: 569–592

Zucker B, Golani G, Kozlov M (2021) Model for ring closure in ER tubular network dynamics. *bioRxiv* https://doi.org/10.1101/2021.11.18.469198 [PREPRINT]

Expanded View Figures
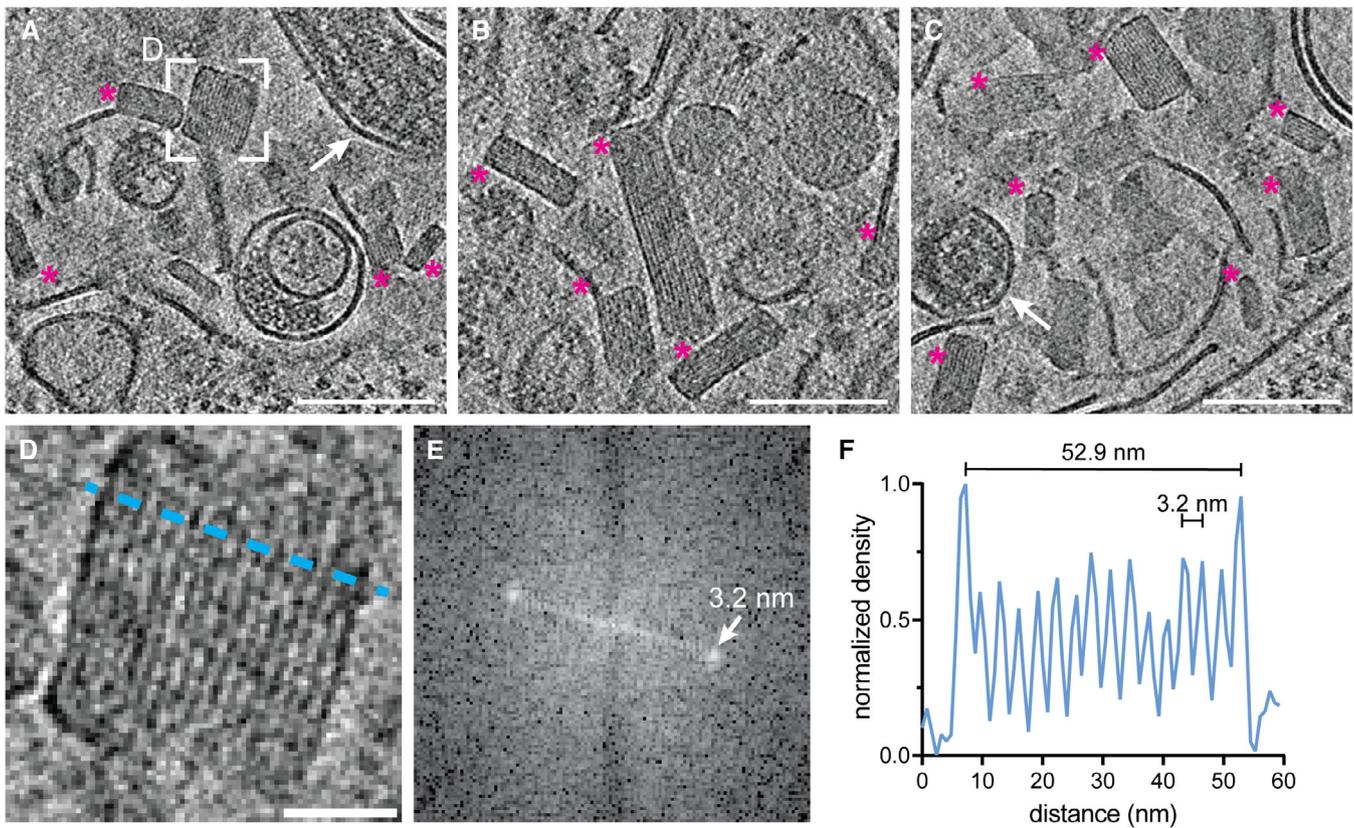
Figure EV1. Crystalline lipidic structures in endosomal compartments of EBOV-infected Huh7 cells.

A–C Slices through tomograms showing lumina of endosomal compartments crowded with crystalline lipidic structures (magenta asterisks). Two virions are highlighted with white arrows in (A) and (C).

D Magnified view of the area highlighted in (A) showing a cross-section through a crystalline lipidic structure. To determine the spacing between the stacked lipid monolayers, a line profile was determined (blue line).

E Fourier-transform analysis of the tomogram slice shown in (D) revealing a spacing of 3.2 nm.

F Line profile across the crystal shown in (D) showing the diameter of the structure along the short axis of 52.9 nm, and the regular 3.2 nm spacing of the lipid monolayers.

Data information: Scale bars: (A–C): 100 nm, (D): 20 nm.
Source data are available online for this figure.
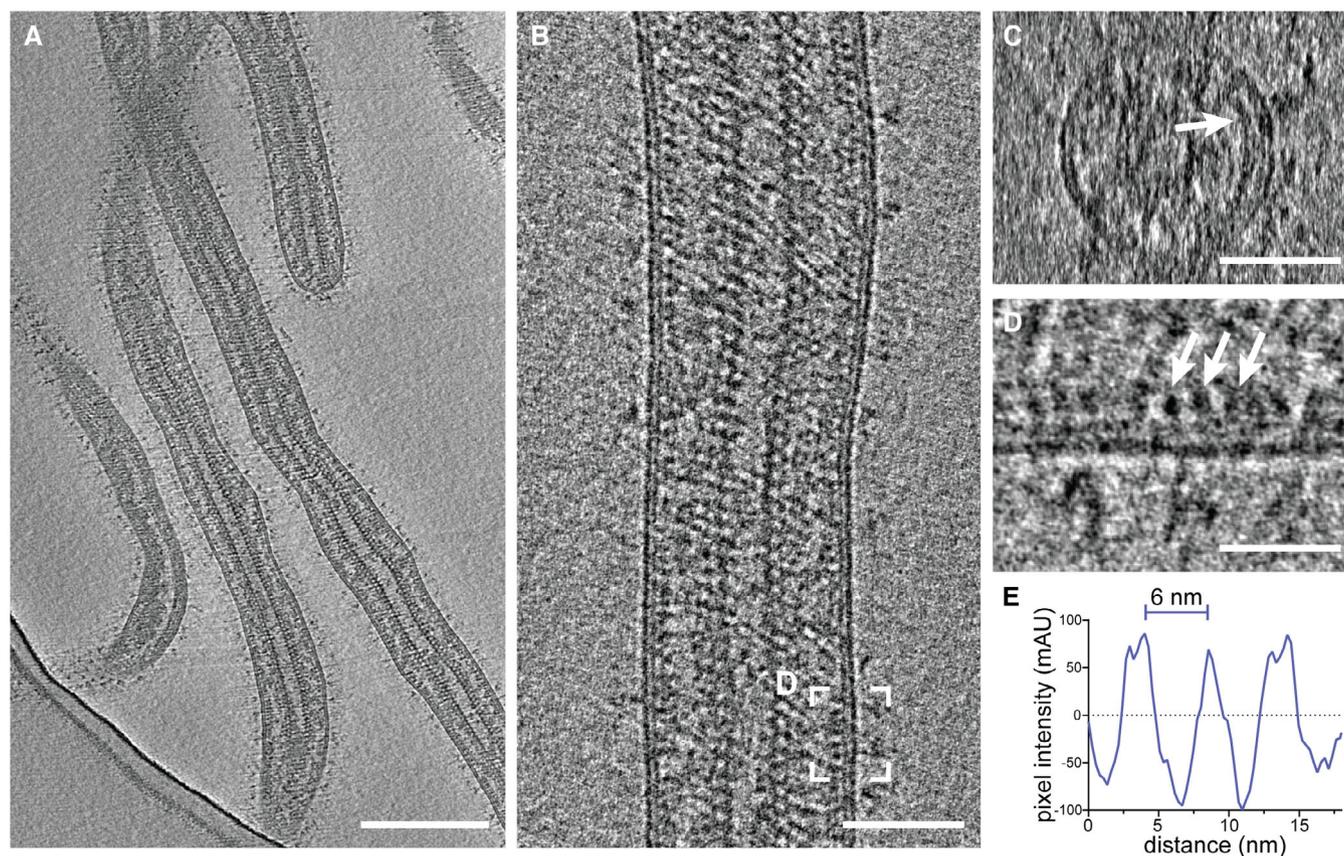
Figure EV2. Cryo-electron tomography of purified and chemically fixed EBOV.

A   Slices through a tomogram showing an overview of filamentous virions. Condensed and decorated nucleocapsids span the length of each virion.

B, C   Longitudinal and transverse cross-section, respectively, of a tomogram containing a filamentous EBOV.

C   Transverse cross-section of the virion shown in (B). The VP40 matrix adjacent to the inner membrane monolayer is highlighted by a white arrow.

D   Magnified area highlighted in (B) showing a longitudinal cross-section of the VP40 densities lining the inner membrane monolayer.

E   Line profile determined adjacent to the inner monolayer of the virion shown in (B) showing the approximately 6 nm pitch of the VP40 matrix.

Data information: Scale bars: (A), (B): 200 nm, (C): 50 nm, (D): 20 nm.
Source data are available online for this figure.
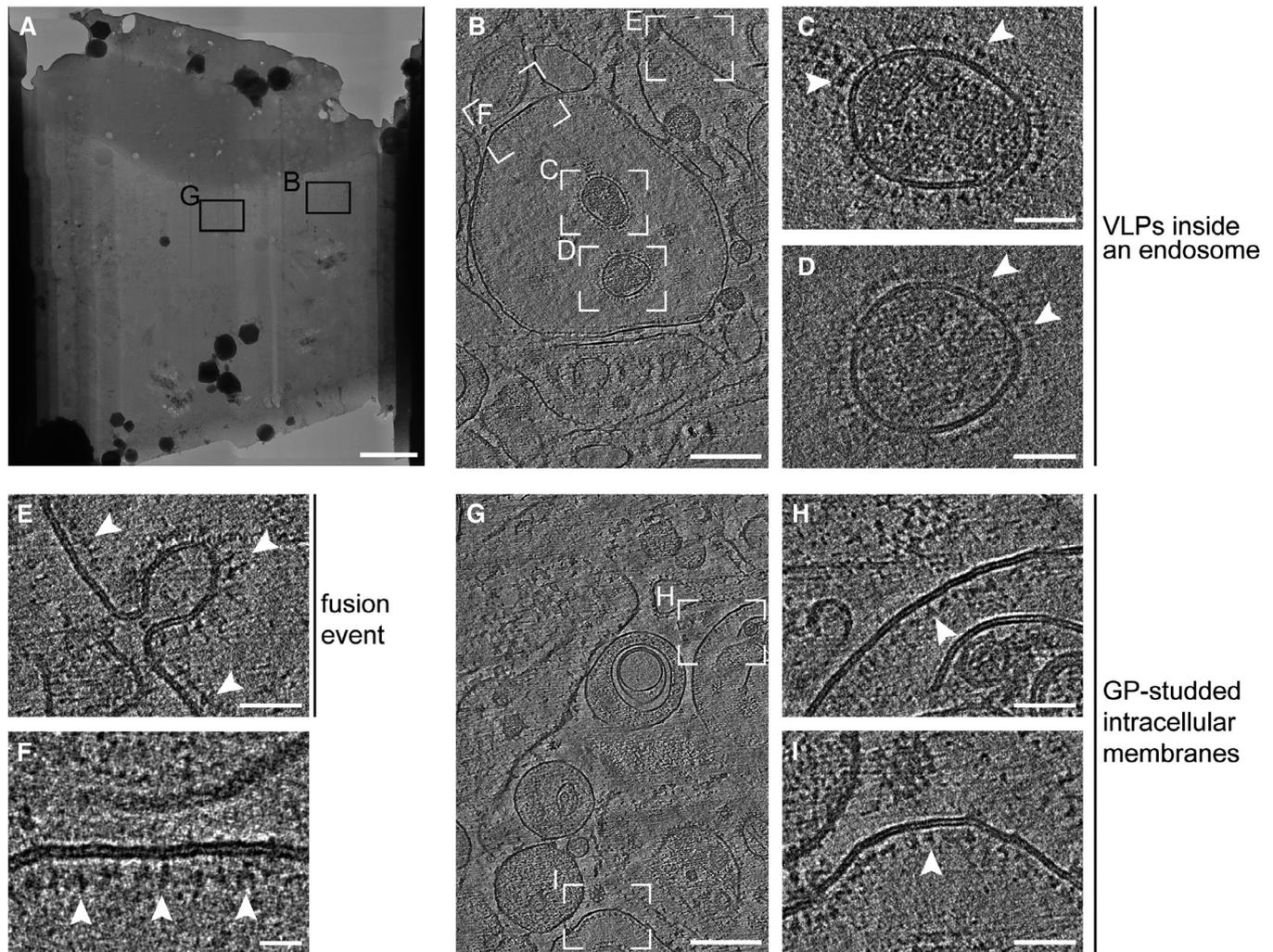
Figure EV3. *In situ* cryo-ET of EBOV VLPs entering Huh7 cells.

A   Overview map of a lamella produced by cryo-FIB milling of an Huh7 cell incubated for 1 h with EBOV VLPs composed of VP40 and GP.
B   Slices through a tomogram taken as indicated in (A).
C, D   Areas highlighted in (B) showing cross-sections of VLPs inside a cellular compartment. The membranes surrounding the particles are studded with GPs (white arrowheads), while the lumina are crowded by disordered protein densities.
E   Area highlighted in (B) showing an invagination studded with GPs (white arrowheads), likely representing a fusion event.
F   Area highlighted in (B) showing a post-fusion event as indicated by the GPs facing the luminal side of the intracellular compartment.
G   Slices through a tomogram taken as indicated in (A) showing post-fusion events characterized by intracellular membranes studded by GPs facing the luminal sites.
H, I   Areas highlighted in (G) showing GP-decorated membranes (indicated by white arrowheads).

Data information: Scale bars: (A): 5 μm, (B), (G): 200 nm, (C–E), (H), (I): 50 nm, (F): 20 nm.
Source data are available online for this figure.
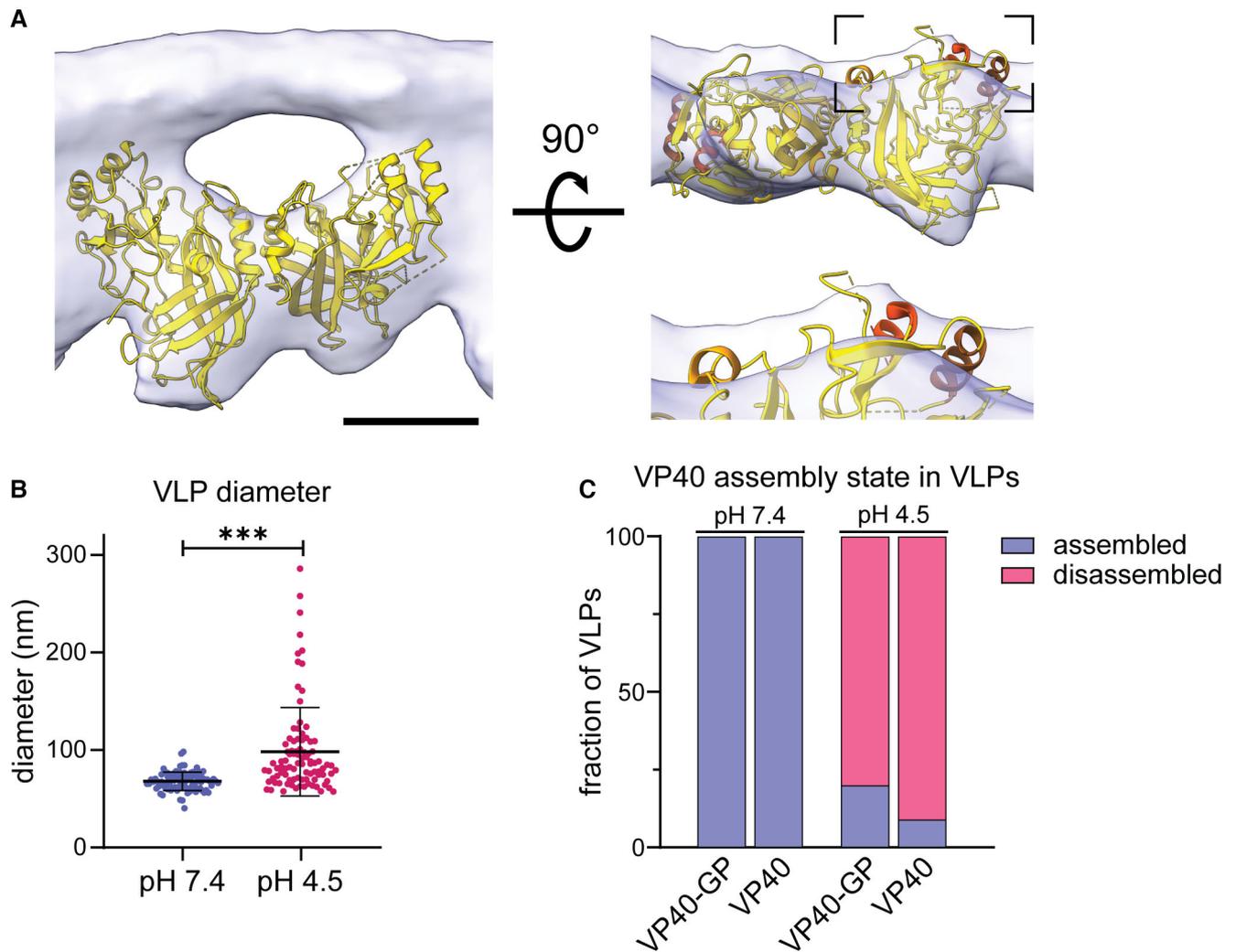
Figure EV4. Structural characterization of the VP40 matrix in VLPs by cryo-ET.

A   VP40 dimer structure (pdb: 7jzj) fitted into the subtomogram average presented in Fig 2 from the side view including the density of the inner VLP monolayer and rotated by 90°. Helical segments protruding from the subtomogram average are highlighted in shades of orange.

B   Diameter of VLPs composed of GP and VP40 measured from membrane-to-membrane after incubation at pH 7.4 and pH 4.5. Asterisks indicate statistical significance as judged by a two-tailed Welch's *t*-test, assuming unequal variance ($P < 0.0001$).

C   Quantification of the VP40 assembly state of VLPs composed of VP40 and GP ($n = 37$ at pH 7.4 and 18 at pH 4.5); or VP40 alone ($n = 22$ at pH 7.4 and 8 at pH 4.5). The VP40 matrix was either assembled (blue), or disassembled (dark pink). VP40 assembly in VLPs subjected to neutral or low pH was assessed by cryo-ET.

Data information: Scale bars: (A) 2.5 nm.

Figure EV5. Characterization of VP40 dimer angles and lipidomics.

A Superimposition of the crystallographic structure (pdb: 7jzj, yellow) with the membrane bound VP40 structure from the MD simulations (blue).

B The area highlighted in (A) shows the missing CDTs residues computationally modeled (green).

C Representation of the rotation angle of VP40 monomers along the NTD-dimerization domain.

D The dihedral angle between VP40 monomers is defined as the angle between the plane containing the vector connecting alpha carbon atoms of L75^{monomer1} and T112^{monomer1} and the vector connecting atoms T112^{monomer1} and T112^{monomer2} and the plane containing this second vector and the vector connecting atoms T112monomer2 and L75monomer2.

E Dihedral angle distribution shows that, regardless of pH, VP40 monomers within the dimer are flexible with a rotation angle oscillating around 1° (SD 9.5) in water, which is 17° smaller than the one measured for the crystallographic structure (pdb: 7jzj). VP40 dimer flexibility is not constrained upon binding to the membrane. However, after binding to the bilayer, the angle distribution was significantly ($P \leq 0.0001$) shifted to a value of 3.7° and 4.5° at pH 7.4 and 4.5, respectively. Unpaired t-tests were performed to evaluate the significance of differences in angle distributions.

F VP40-membrane internal energy calculated as the sum of short-range Coulomb and Lennard-Jonson interactions at neutral (orange) and low (red) pH. The internal energies have been calculated over the last 100 ns of the biased MD simulation windows centered at the membrane distance where the free energy minima were reconstructed (3.0 nm and 2.7 nm for neutral and low pHs, respectively). The error was estimated using the block averages over 5 blocks.

G Abundance of low-abundant lipids in the envelope of Ebola VLPs composed of GP, VP40, NP, VP24 and VP35. The mean abundance in mol% and values for each experiment ($n = 3$ biological replicates) are plotted together with the standard error of the mean (red). phosphatidylinositol (PI), phosphatidylglycerol (PG), phosphatidic acid (PA), ceramide (Cer), hexosylceramide (HexCer), cholesterol ester (CE) diacylglycerol (DAG), triacylglycerol (TAG). Prefix "a" indicates acyl-linked glycerophospholipids, prefix "e" indicates ether-linked (plasmanyl) or the presence of one odd and one even chain fatty acyl.

H Sequence alignment of VP40 proteins (amino acids 223–280) from all EBOV species (EBO) and Marburg virus (MAV). For each sequence, the uniprot identifiers are given on the left and the Ebolavirus species are indicated as ZM: Zaira Mayinga EBOV, SU: Sudan EBOV, RR: Reston EBOV, BB: Bundibugyo EBOV, TF: Tai Forest EBOV, B: Bombali virus. Conserved hydrophobic and hydrophilic amino acids are highlighted according to the color scheme of (Kyte & Doolittle, 1982). The hydrophilic amino acids K224, K225, K274 and K275 (indicated by arrows) are highly conserved among the EBOV species.

Figure EV5.

Appendix

The Ebola virus VP40 matrix layer undergoes endosomal disassembly essential for membrane fusion

Sophie L. Winter[1,2], Gonen Golani[2,3], Fabio Lolicato[4,5], Melina Vallbracht[1,2], Keerthihan Thiyagarajah[1,2], Samy Sid Ahmed[6], Christian Lüchtenborg[4], Oliver T. Fackler[6,7], Britta Brügger[4], Thomas Hoenen[8], Walter Nickel[4], Ulrich S. Schwarz[2,3], Petr Chlanda[1,2]*

[1] Schaller Research Groups, Department of Infectious Diseases, Virology, University Hospital Heidelberg, Heidelberg, Germany
[2] BioQuant-Centre for Quantitative Biology, Heidelberg University, Heidelberg, Germany
[3] Institute for Theoretical Physics, Heidelberg University, Heidelberg, Germany
[4] Heidelberg University Biochemistry Center, Heidelberg, Germany
[5] Department of Physics, University of Helsinki, Helsinki, Finland
[6] Department of Infectious Diseases, Integrative Virology, University Hospital Heidelberg, Heidelberg, Germany
[7] German Centre for Infection Research (DZIF), Partner Site Heidelberg, Germany
[8] Institute of Molecular Virology and Cell Biology, Friedrich-Loeffler-Insitut, Greifswald-Insel Riems, Germany

*Correspondence: chlanda@bioquant.uni-heidelberg.de

Table of Contents

26
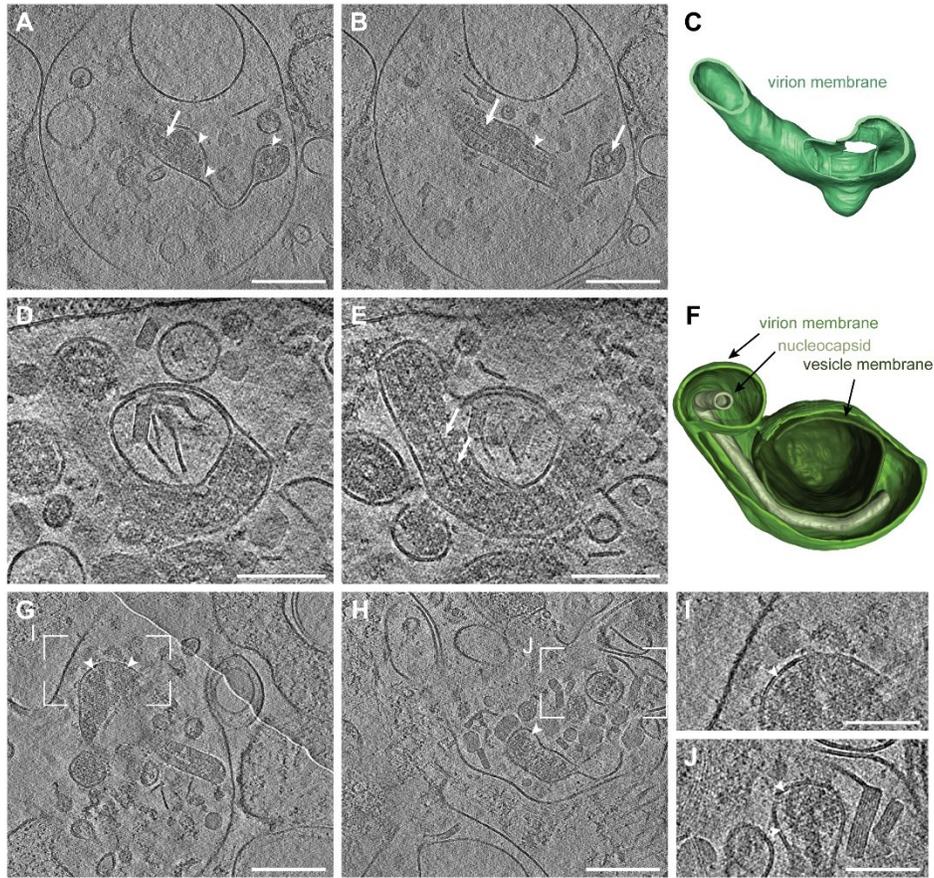
Appendix Figure S1

In situ cryo-ET of EBOV infecting Huh7 cells. Slices through tomograms showing Ebola virions inside late endosomal compartments. All virions display condensed nucleocapsids (white arrows) and disassembled VP40 layers, which have detached from the viral membrane as apparent from the gap adjacent to the inner lipid monolayer (white arrowheads). **(A-B)** Different slices through the same tomogram showing an internalized EBOV with a disassembled VP40 matrix and highly flexible membrane. The nucleocapsid is still condensed (white arrow). **(C)** 3D segmentation of the lipid envelope of the EBOV virion (green) shown in (A) and (B). **(D-E)** Different slices through the same tomogram showing an internalized EBOV virion with a disassembled VP40 matrix and condensed nucleocapsid. The virion had engulfed an intraluminal vesicle containing cholesterol ester crystals, indicating that this virus has undergone fusion. **(F)** 3D segmentation of EBOV shown in (D) and (E) showing the viral membrane (green), nucleocapsid (light green) and vesicle membrane (dark green). Scale bars: (A), (B): 200 nm, (D-J): 100 nm.

41
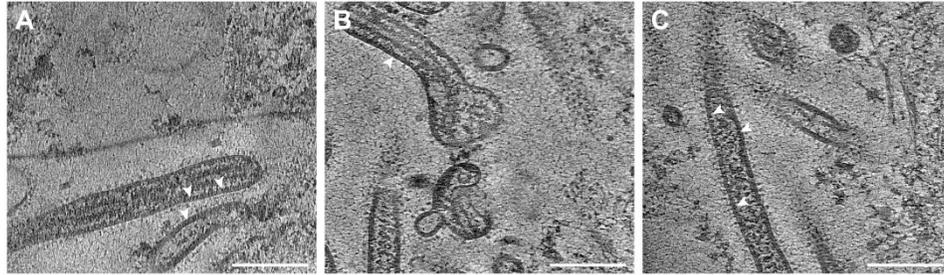
Appendix Figure S2

In situ cryo-ET of budding and released EBOV from infecting Huh7 cells. (A-C) Slices through tomograms showing Ebola virions adjacent to the plasma membrane of infected Huh7 cells. All virions contain assembled VP40 layers as apparent from the regular densities decorating the inner lipid monolayer at the luminal side (white arrowheads). Scale bars: 200 nm.

48
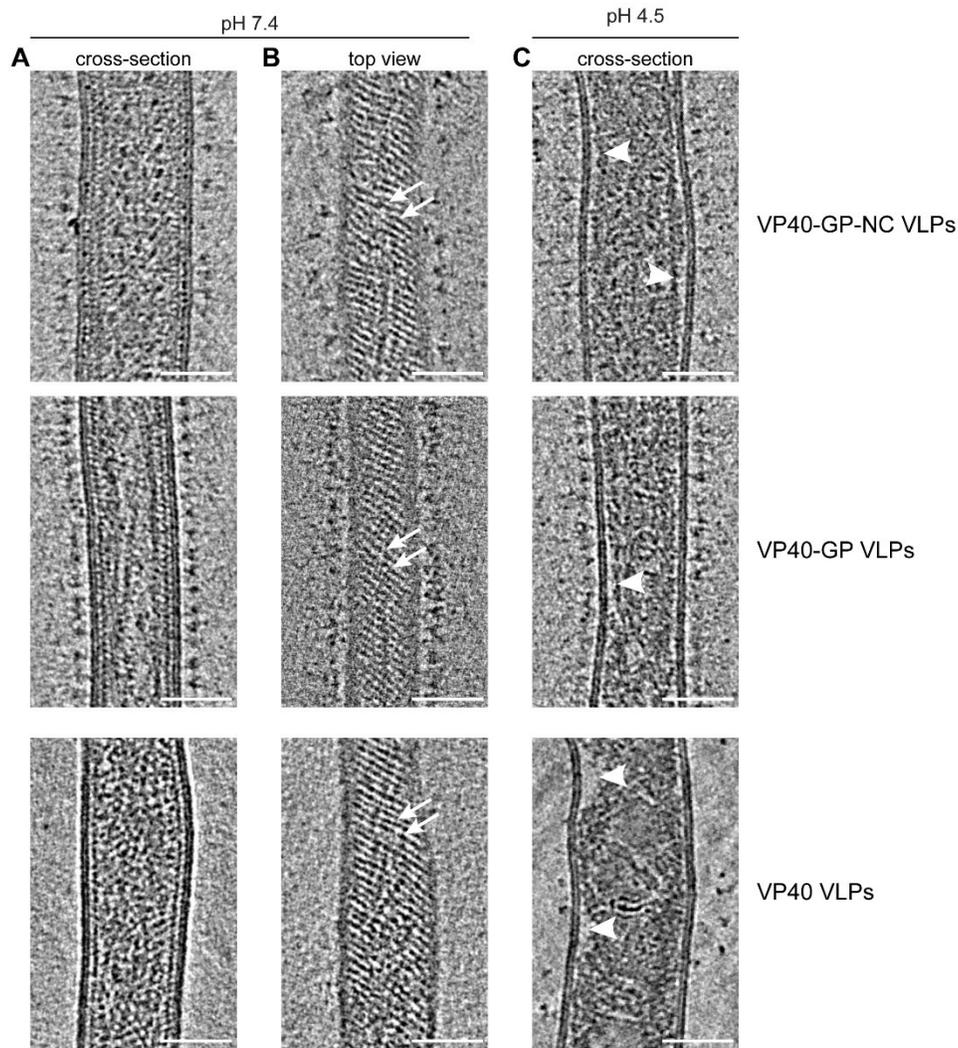
Appendix Figure S3

Structural characterization of unpurified EBOV VLPs of different protein composition. From top to bottom, the VLPs are composed of VP40, GP and the nucleocapsid (NC) proteins NP, VP24 and VP35; VP40 and GP; and VP40 alone. **(A)** Cross-sectional slices through tomograms showing filamentous VLPs at pH 7.4. **(B)** Near-to-surface slices of tomograms showing the top view of VLPs incubated at pH 7.4 and exhibiting the characteristic striations of the VP40 matrix (white arrows). **(C)** Cross-sectional slices through tomograms showing VLPs incubated at pH 4.5. No ordered VP40 matrix is visible adjacent to the VLP membrane as indicated by white arrowheads. Scalebars: 50 nm.

58
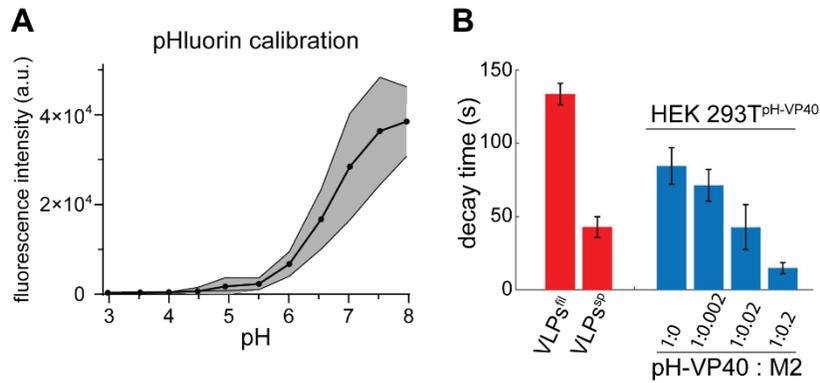
Appendix Figure S4

Calibration of pHluorin fluorescence and decay times. (A) Fluorescence intensity of HEK 293T cells expressing pHluorin-VP40 measured at 488 nm as a function of pH. Cells were grown in cell culture media before exchanging the media with HNE buffer (10 mM HEPES, 100 mM NaCl, 1 mM EDTA) at different pH. **(B)** pH characteristic decay times as found by fitting the pH levels to Eq. 3 of VLPs (red) and HEK 293T cells (blue) expressing pHluorin-VP40 and influenza M2 in increasing M2 levels. Filamentous VLPs 134±7 sec (n=154), spherical VLPs 43±7 sec (n=66), cells expressing VP40 only 84±12 sec (n=44), cells expressing VP40 and M2 at 1:0.002 molar ratio 71±11 sec (n=30), cells expressing VP40 and M2 at 1:0.02 molar ratio 43±15 sec (n=28), cells expressing VP40 and M2 at 1:0.2 molar ratio 15±4 sec (n=26).

69
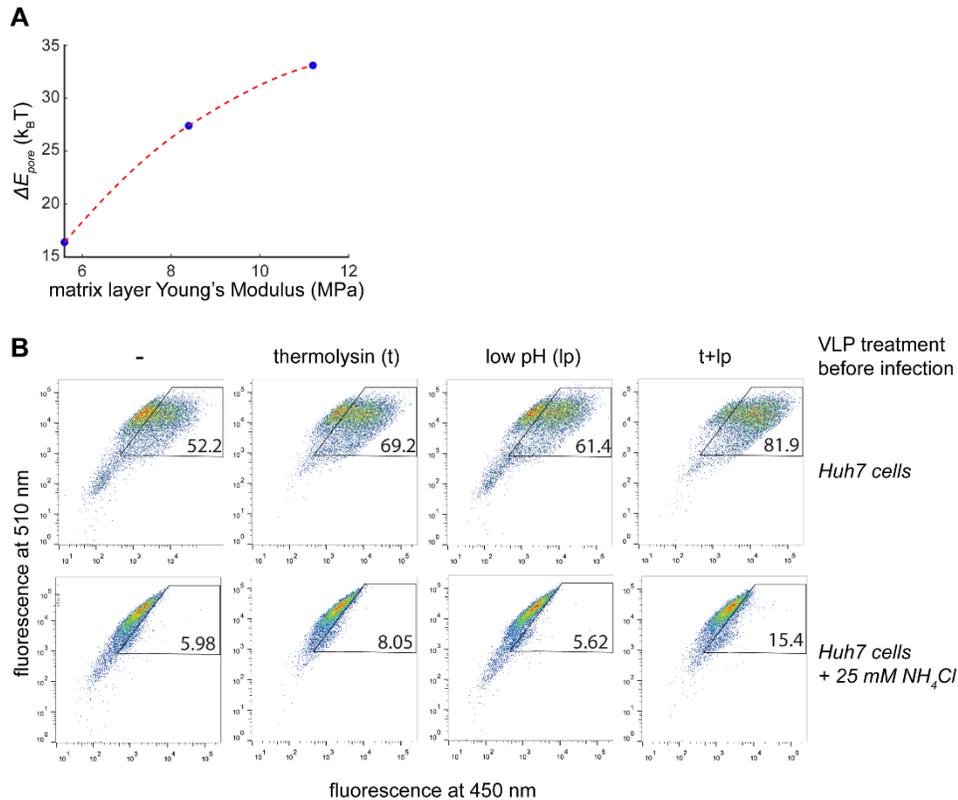
Appendix Figure S5

Entry of Ebola BlaM-VLPs into Huh7 cells. (A) Plot showing the dependence of the change in fusion pore formation energy between $u\_0=38$ k_BT/nm^2 to $u\_0=0$ (ΔE_pore) on the matrix layer Young's modulus. Dotted lines serve as a guide to the eye. **(B)** FACS plots showing virus entry as measured by a fluorescence shift of infected cells from emission at 510 nm (no entry) to 450 nm (entry). The top row indicates in vitro VLP treatments prior to infection including buffer control (-), thermolysin treatment, low pH treatment, and a combination of thermolysin and low pH. The first row of FACS data shows entry into Huh7 target cells, the second row shows entry into Huh7 cells treated with 25 mM ammonium chloride to neutralize acidic compartments and assess virus entry in the absence of acidification. FACS data are shown from one out of three repetitions, with 10000 cells measured per sample.